Double Z-scheme $FeVO_4/Bi_4O_5Br_2/BiOBr$ ternary heterojunction photocatalyst for simultaneous photocatalytic removal of hexavalent chromium and rhodamine B

Auttaphon Chachvalvutikul[a], Tawanwit Luangwanta[a], Sulawan Kaowphong[a,b,c,*]

[a] Department of Chemistry, Faculty of Science, Chiang Mai University, Chiang Mai 50200, Thailand

[b] Center of Excellence in Materials Science and Technology, Chiang Mai University, Chiang Mai 50200, Thailand

[c] Materials Science Research Center, Faculty of Science, Chiang Mai University, Chiang Mai 50200, Thailand

* Corresponding author

E-mail : sulawank@gmail.com; sulawan.k@cmu.ac.th

Tel: +66 (0)53 943341

Abstract

Hypothesis

Fabrication of the heterojunction photocatalyst with appropriate band potentials as a promising method of inhibiting electron-hole pair recombination leading to enhanced photocatalytic properties.

Experiments

Herein, BiOBr, $Bi_4O_5Br_2$, and binary BiOBr/$Bi_4O_5Br_2$ composite were selectively synthesized by employing a one-step microwave irradiation method. Then, double Z-scheme $FeVO_4$/$Bi_4O_5Br_2$/BiOBr ternary composites with different weight percentages (%wt) of $FeVO_4$ were fabricated and their photocatalytic applications were studied. The photodegradation of organic compounds (rhodamine B (RhB), methylene blue (MB) and salicylic acid (SA)), along with the photoreduction of hexavalent chromium (Cr(VI)) were investigated.

Findings

Comparing with the single and binary photocatalysts, and a commercial TiO_2, the 1%wt-$FeVO_4$/$Bi_4O_5Br_2$/BiOBr photocatalyst demonstrated superior visible-light-driven photocatalytic performance. In a Cr(VI)/RhB combined system, Cr(VI) photoreduction was further improved and coexisting RhB molecules were simultaneously degraded. Removal of Cr(VI) and RhB were maximized by adjusting both pH values and catalyst dosages. Based on UV-vis diffuse reflectance spectroscopy, photoluminescence spectroscopy, electrochemical investigations, active-species trapping, nitrotetrazolium blue transformation, and silver photo-deposition experiments, a double Z-scheme charge transfer mechanism with an RhB-sensitized effect was proposed. This special mechanism has led to significant enhancement in charge segregation and migration, along with higher redox properties of the ternary composite, which were responsible for the excellent photocatalytic activity.

Keywords: Ternary heterojunction; Double Z-scheme; Dye-sensitization; Cr(VI) photoreduction; Photodegradation; Microwave irradiation method

1. Introduction

With massive increases in water pollution, the removal of pollutants from water bodies has become a critical issue. This can be accomplished through various techniques such as adsorption [1], photocatalysis [2,3], and electrocatalysis [3]. Semiconductor photocatalysis is a promising technology that can be used to address the environmental pollution that is related to organic and inorganic pollutants in industrial wastewater. In order to fully utilize renewable and clean solar energy, which is mainly comprised of visible light, there have been significant attempts to develop and synthesize visible-light active photocatalysts [4,5]. Bismuth oxyhalides (BiOX, X = Cl, Br and I) have exhibited striking photocatalytic activities due to their layered structures with [Bi_2O_2] slabs interleaved by double slabs of halide atoms. Such layered structure induces an internal static electric field, which then facilitates segregation of electron-hole pairs and favors an enhanced photocatalytic activity [6–9]. Among them, bismuth oxybromide (BiOBr) exhibited the highest photocatalytic activity due to its relatively high photo-oxidation power of the photoactivated holes [10–13]. However, this photocatalyst usually suffers from a low absorption efficiency in the visible light region, which can limit the utilization of visible light to generate electron-hole pairs.

Density functional theory (DFT) calculations [14] indicated that the valence band of BiOBr is mainly occupied by O 2*p* and Br 4*p* hybrid orbitals and its conduction band is composed of Bi 6*p* orbital. This suggests that tuning bismuth and bromide contents in BiOBr could modulate its band edge potentials, and consequently change its band gap energy. In addition, bismuth-rich strategy strengthens the hybridization of the conduction band and reinforces the internal static electric field, which in turn promotes electron migration and

segregation of the photoactivated electron–hole pairs. Therefore, the bismuth-rich strategy has received significant interest over its potential to improve the photocatalytic performance of BiOBr. Bismuth-rich BiOBr photocatalysts have been previously reported with a narrow band gap and for possessing higher visible light absorption properties than the ordinary BiOBr material [15]. $Bi_4O_5Br_2$, one of the known bismuth-rich BiOBr materials, exhibited higher visible-light-driven photocatalytic activity than BiOBr in terms of the degradation of bisphenol A [16,17], resorcinol [18], rhodamine b [19], and ciprofloxacin [20], as well as in the photocatalytic reduction of CO_2 [21]. Although $Bi_4O_5Br_2$ exhibited strong visible light photocatalytic properties, its quantum efficiency is still rather poor due to undesirable electron-hole recombination [22]. Therefore, there is need to improve the lifetime of the photoactivated electron-hole pairs in an attempt to overcome the unsatisfied quantum efficiency of the material.

Some previous publications [23,24] have reported that the BiOBr/$Bi_4O_5Br_2$ heterojunction photocatalyst exhibited significant enhancement in photocatalytic activity due to a suitable band alignment that ultimately led to an effective charge separation between the two individual semiconductors. However, the synthesis of the BiOBr/$Bi_4O_5Br_2$ heterostructure required harsh synthetic conditions [18,19,25–28]. For example, at high temperature, $Bi_4O_5Br_2$ was produced from a gradual loss of bromide ion in the BiOBr crystal accompanied by phase transformations [24]. Compared with the binary heterojunction system, a ternary heterojunction system had greatly satisfied electron-hole pair separation efficiency and much prolonged the charge carrier's lifetime, both of which resulted from the multistep charge-transfer processes and led to better photocatalytic activity [29,30]. In this research work, the iron (III) vanadate, $FeVO_4$, was chosen as a visible-light photosensitizer for the construction of the ternary $FeVO_4$/$Bi_4O_5Br_2$/BiOBr heterostructures owing to its narrow energy band gap, visible-light active properties, and high stability [31,32]. Moreover, according to the outcomes

of our previous studies [33,34], we also found that by coupling the optimum content of $FeVO_4$ with bismuth-based compounds, compatible electronic band structure alignments can be formed at the interface between the individual semiconductors to exhibit the enhancement of photocatalytic activity. This likely would have resulted from the effective segregation of the charge carriers and led to improved visible light responsibility.

Herein, we firstly synthesized the binary $BiOBr/Bi_4O_5Br_2$ composite using the facile one-step microwave irradiation method. After that, the synthesized $BiOBr/Bi_4O_5Br_2$ composite was hybridized with $FeVO_4$ using the wet-impregnation method to fabricate the ternary $FeVO_4/Bi_4O_5Br_2/BiOBr$ composites. The weight percentages (%wt) of $FeVO_4$ in the ternary composites were varied in order to enhance their photocatalytic activities, which were then investigated by the photocatalytic degradation of organic pollutants under visible light irradiation. Using $FeVO_4/Bi_4O_5Br_2/BiOBr$ composite with an optimum %wt of $FeVO_4$, we also investigated its photocatalytic performance towards the photoreduction efficiency of Cr(VI). Since the co-existence of organic and inorganic pollutants is commonly found in real industrial wastewater, for example, the coexistence of Cr(VI) and dyes/non-dyes in the effluents from the leather tanning process [35–37], we further investigated the photoreduction of Cr(VI) in the Cr(VI)/RhB combined pollution system. A series of experiments under the combined pollution system was carried out to optimize photocatalytic conditions. Possible charge transfer and photocatalytic mechanisms for the removal of Cr(VI) and RhB in the combined pollutant system were discussed in detail.

2. Experimental procedures

2.1. Synthesis of photocatalysts

$FeVO_4$ was synthesized using a similar method to that which had been used in our previous publications [33,34]. For the synthesis of bismuth oxybromide photocatalysts,

$Bi(NO_3)_3 \cdot 5H_2O$ (1 mmol; Sigma-Aldrich, Co., 95%) and KBr (1 mmol; RCI Labscan Limited, 99.9%) were separately dissolved in 20.0 mL of ethylene glycol (Carlo Erba Reagents, 99.5%) and then mixed for 30 min. Next, the mixed solution was irradiated using 2.45 GHz microwave radiation operated at 600 W for 8, 60, and 110 cycles in order to obtain BiOBr, BiOBr/$Bi_4O_5Br_2$ binary heterostructure, and $Bi_4O_5Br_2$, respectively. Each cycle was performed at 30-s on at every 90-s interval. The obtained powder was filtered, washed with deionized water, and dried at 70 °C overnight.

For the preparation of ternary $FeVO_4$/$Bi_4O_5Br_2$/BiOBr composites, a certain amount of $FeVO_4$ powder was dispersed in 40.0 mL of methanol (RCI Labscan Limited, 99.9%) and kept under sonication for 30 min. Then, a certain amount of the BiOBr/$Bi_4O_5Br_2$ powder was added into the suspension and was constantly stirred at room temperature for 24 h. Finally, the obtained powder was dried at 70 °C and heated at 200 °C for 30 min. The $FeVO_4$/$Bi_4O_5Br_2$/BiOBr composites were then denoted as xFV/Br where x represents the weight percentages of $FeVO_4$ (0.5, 1, 3, 6.25 and 12.5%wt) and Br represents the BiOBr/$Bi_4O_5Br_2$ host material. For the purposes of comparison, a physical mixing sample, denoted as PM, was also prepared by grinding the $FeVO_4$ powder with the BiOBr/$Bi_4O_5Br_2$ powder.

2.2. Characterizations

X-ray diffraction spectroscopy (XRD, Rigaku Smartlab) was used to investigate the purity, structure and crystallinity of the powders. Chemical compositions and oxidation states of the constituent elements were determined by X-ray photoelectron spectroscopy (XPS, AXIS Ultra DLD, Kratos Analytical Ltd.) using Al Kα X-ray source at 1.4 keV radiation. XPS spectra were corrected by referencing the binding energy of an adventitious carbon (C 1*s*) peak at 284.6 eV. Morphology, microstructure and the elemental composition of the samples were

investigated with the use of a field emission scanning electron microscope (FESEM, JEOL JSM-6335F) and a transmission electron microscope (TEM, JEOL JEM-2010). These were used in conjunction energy dispersive X-ray spectrometry (EDS). Optical properties were examined by UV-vis diffuse reflectance spectroscopy (UV-vis DRS, UV-1800 Shimadzu) that was equipped with a specular reflectance measurement attachment. The results were referenced against $BaSO_4$. Photoluminescence (PL) spectra were recorded using a photoluminescence spectrometer (PL, Avantes Avaspec-2048TEC-USB2) with an excitation wavelength of 345 nm. Zeta potential of the ternary composite was measured on a Zetasizer (Malvern Nano ZS). The Brunauer-Emmett-Teller N_2 gas adsorption (BET, Quantachrome, Quadrasorb-*evo*) and the Barret–Joyner–Halenda (BJH) methods were used to determine the surface area, pore radius, and total pore volume of the samples. Inductively coupled plasma-optical emission spectroscopy (ICP-OES; Perkin Elmer 4300 DV) was used to determine Fe and V ions leaching in the supernatant solution sample.

2.3. Photocatalytic experiments

To investigate the optimum content of $FeVO_4$ in the ternary composite, the synthesized xFV/Br sample (100 mg) was dispersed in aqueous solutions (200.0 mL) of organic dye (methylene blue; MB and rhodamine B; RhB, 10 ppm) and a colorless organic compound (salicylic acid; SA, 10 ppm). The MB, RhB and SA compounds with a purity of 99.0% were purchased from Fluka, Riedel-de Haën and Sigma Aldrich, respectively. Prior to employing light irradiation, the suspension was stirred in the dark for 30 min to reach an adsorption-desorption equilibrium. The suspension was exposed to visible light generated from a 50 W white light-emitting diode lamp (LED, YNL Model COB LED CHIP). At each given time interval, the suspension was taken out and separated by centrifugation. The remaining concentration of the organic compound was analyzed using a UV-vis spectrophotometer (UV-

vis, UV-1800 Shimadzu) by measuring the absorption intensity at its maximum absorption wavelength (λ_{max} = 664, 554 and 294 nm for MB, RhB and SA, respectively). A control experiment was also carried out without adding the photocatalyst. The photodegradation efficiency (%DE) was calculated using the following equation;

$$\%DE = \frac{C_0 - C}{C_0} x\ 100$$

where C_0 and C represent the concentrations of the target pollutants when the adsorption-desorption equilibrium was achieved, and after being exposed to the light irradiation, respectively. The photocatalytic reaction kinetic was investigated using the pseudo-first order kinetic model as follows;

$$\ln \frac{C_0}{C} = k_{\mathrm{app}} t$$

where k_{app} represents the apparent pseudo-first order rate constant (min^{-1}).

The ternary $FeVO_4/Bi_4O_5Br_2/BiOBr$ composite with an optimum content of $FeVO_4$ was applied for the determination of the photoreduction of Cr(VI) ion in the $K_2Cr_2O_7$ solution (200.0 mL, 20 and 30 ppm; Sigma-Aldrich, 99.0%). The suspension was stirred in the dark (30 min) to make sure that adsorption-desorption equilibrium was established. The remaining concentration of the $K_2Cr_2O_7$ solution was monitored using the diphenylcarbazide (DPC) method in which the absorption intensity of the Cr(VI)-DPC complex was measured at 540 nm. The photoreduction efficiency (%RE) and the k_{app} value were also calculated in the same way by using the photodegradation efficiency calculation. All the photocatalytic data are based on the average values of three parallel experiments.

In addition, this photocatalyst was also applied in a mixed solution of $K_2Cr_2O_7$ (30 ppm) and RhB (5, 10, or 20 ppm) to a total volume of 200.0 mL. Before treating the suspension with the DPC method, an absorbance of 554 nm was measured to monitor the photodegradation of RhB. For the accurate quantification of Cr(VI), the interference caused by the absorption of

RhB was eliminated by subtracting the absorbance at 540 nm of the suspension containing Cr(VI) and RhB (the suspension before DPC reagent was added (Sigma-Aldrich, >99.0%)) from the absorbance at 540 nm of the Cr(VI)-DPC complex. A series of experiments were also conducted by varying photocatalyst dosages and adjusting pH values with 1 M HNO_3 (Sigma-Aldrich, 70.0%) or 1 M NH_4OH (QRëC™, 25%), in order to optimize the operation parameters.

Trapping experiments were carried out using 1 mM of various scavengers including ascorbic acid (ASC; Merck, 99.0%) [11], ethylenediaminetetraacetic acid disodium salt (EDTA-2Na; Sigma-Aldrich, 99.0%) [11], isopropanol (QRëC™, 99.7%) [38] and potassium dichromate ($K_2Cr_2O_7$) [39]) to trap superoxide radicals ($O_2^{\bullet-}$), holes (h^+), hydroxyl radicals ($HO^\bullet$) and photoexcited electrons (e^-), respectively. The nitrotetrazolium blue (NBT) transformation method [40] and the terephthalic acid photoluminescence (TA-PL) probing technique [41] were also used to further confirm the detection of $O_2^{\bullet-}$ and $HO^\bullet$ radicals generated during the photocatalytic reaction.

The silver (Ag) photo-deposition experiment was carried out to further confirm the charge transfer pathway in the ternary $FeVO_4/Bi_4O_5Br_2/BiOBr$ heterojunction. The procedure of this experiment is explained as follows. First, the photocatalyst (20 mg) was dispersed in $AgNO_3$ solution (1 mM, 100.0 mL; Loba Chemie, 99.9%) under visible light irradiation for 360 min. Then, the photocatalyst was collected after Ag was photo-deposited was collected. It was then washed several times with deionized water, and dried. The depositing of Ag on the surface of the ternary heterostructure was then investigated by TEM.

2.4. Electrochemical analyses

All electrochemical measurements were carried out in a standard three electrode system on a Metrohm Autolab Potentiostat/galvanostat (PGSTAT128N, Metrohm Siam Ltd.). The measurement process utilized a working electrode as a photocatalyst coated on a fluorine-

doped tin oxide (FTO) coated sheet of glass, a counter electrode as a platinum (Pt) wire, a reference electrode as Ag/AgCl (3.0 M KCl), and an electrolyte as 0.5 M Na_2SO_4 (pH ~ 6). The electrochemical impedance spectra (EIS) were recorded under an alternating current (AC) voltage at a bias potential of 1.5 V (*vs.* Ag/AgCl) with an amplitude of 0.05 V and a frequency range of 0.01 to 10^5 Hz. Mott-Schottky measurements were performed at a fixed frequency of 10 Hz and an AC amplitude of 10 mV. The transient photocurrent responses were recorded at a fixed applied potential of 1.0 V (*vs.* Ag/AgCl) under visible light irradiation generated from two 50 W LED lamps. To convert the Ag/AgCl (3.0 M KCl) scale to a normal hydrogen electrode (NHE) scale (pH = 0), the following equation was applied;

$$E_{NHE} = E_{Ag/AgCl} + E°_{Ag/AgCl\ (3.0\ M\ KCl)} = E_{Ag/AgCl} + 0.210\ V\ (25\ °C).$$

3. Results and Discussion

3.1. Structural characterization

XRD patterns of the synthesized BiOBr, $Bi_4O_5Br_2$, and BiOBr/$Bi_4O_5Br_2$ powders are illustrated in **Fig. 1**(a). All detectable diffraction peaks of the BiOBr powder matched well with the tetragonal phase of BiOBr (Joint Committee of Powder Diffraction Standards (JCPDS) number 01-085-0862). The diffraction peaks of the $Bi_4O_5Br_2$ powder corresponded to the monoclinic phase of $Bi_4O_5Br_2$ (JCPDS number 00-037-0699 and Inorganic Crystal Structure Database (ICSD) number 94498). The XRD pattern of the binary BiOBr/$Bi_4O_5Br_2$ composite was composed of the characteristic peaks of both tetragonal BiOBr and monoclinic $Bi_4O_5Br_2$ phases. The formation of bismuth-rich $Bi_4O_5Br_2$ could be a consequence of the raised temperature in the reaction system that occurred during the microwave heating process. At a given microwave power, increasing microwave irradiation cycles to 60 and 110 cycles resulted in an increase in the reaction temperature [42], which could then enable the loss of bromide ion in the BiOBr crystal.

XRD patterns of the ternary $FeVO_4/Bi_4O_5Br_2/BiOBr$ composites in comparison with $FeVO_4$ and binary $BiOBr/Bi_4O_5Br_2$ composite are presented in **Fig. 1**(b). The diffraction pattern of $FeVO_4$ is in good accordance with the triclinic $FeVO_4$ structure (JCPDS number 00-038-1372). No impurity peaks were observed suggesting that BiOBr, $Bi_4O_5Br_2$, $BiOBr/Bi_4O_5Br_2$ and $FeVO_4$ were successfully synthesized through the cyclic microwave heating route. In cases of the ternary $FeVO_4/Bi_4O_5Br_2/BiOBr$ composites with 0.5, 1 and 3%wt of $FeVO_4$, the XRD patterns exhibited only the characteristic peaks of BiOBr and $Bi_4O_5Br_2$ owing to much lower contents of $FeVO_4$ as well as a lower diffraction intensity when compared with those of BiOBr and $Bi_4O_5Br_2$. Upon adding more $FeVO_4$ (6.25 and 12.5%wt), the major diffraction peaks of $FeVO_4$ at 27.1° and 27.7° indexing to $(01\bar{2})$ and $(\bar{2}20)$ planes became detectable.

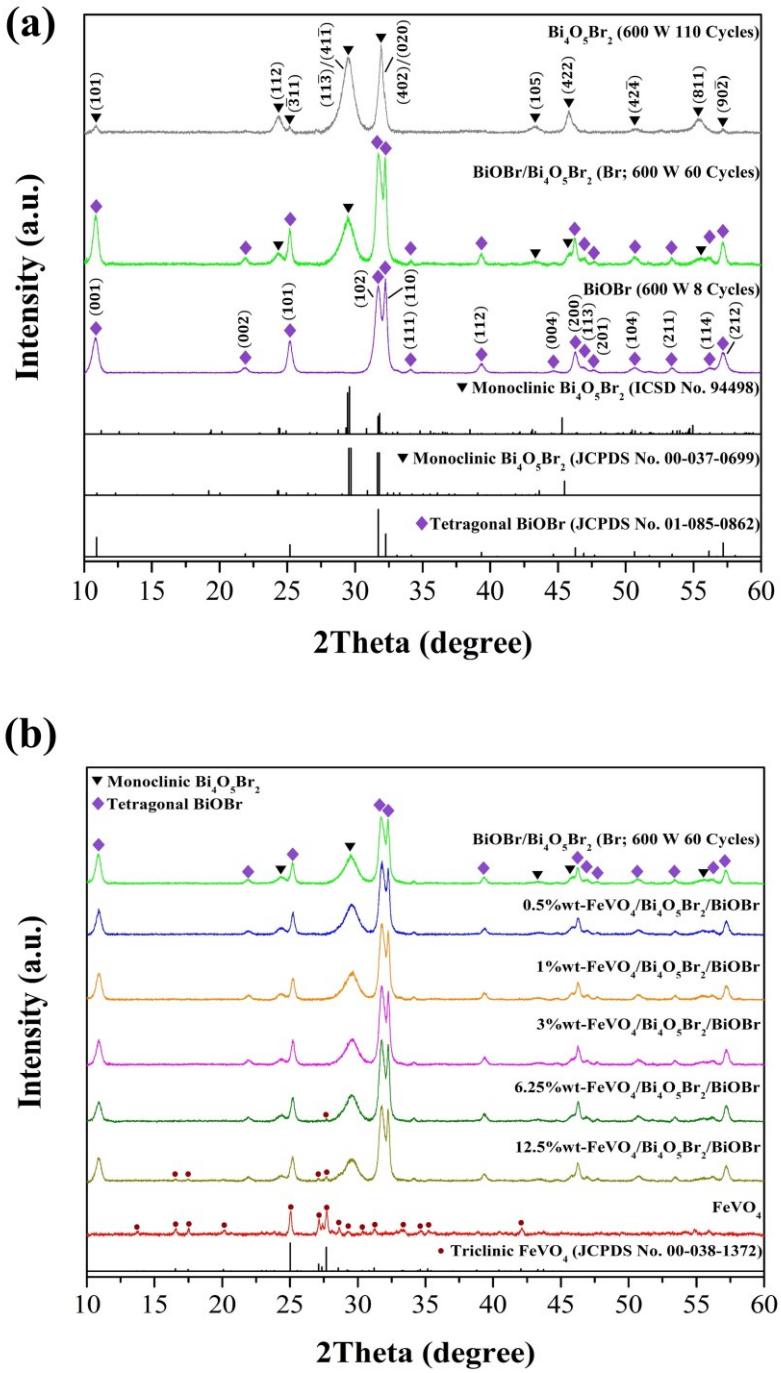

Fig. 1. XRD patterns of (a) BiOBr, $Bi_4O_5Br_2$, and BiOBr/$Bi_4O_5Br_2$ powders synthesized using different microwave irradiation cycles, and (b) $FeVO_4$, BiOBr/$Bi_4O_5Br_2$, and $FeVO_4$/$Bi_4O_5Br_2$/BiOBr nanocomposites with different loading amounts of $FeVO_4$.

XPS spectra of $FeVO_4$, BiOBr/$Bi_4O_5Br_2$, and 1%wt-$FeVO_4$/$Bi_4O_5Br_2$/BiOBr are shown in **Fig. 2**. The survey spectrum of $FeVO_4$/$Bi_4O_5Br_2$/BiOBr (**Fig. 2**(a)) indicated that the peaks

belonging to Bi, O, Br, Fe, and V elements were observed. **Fig. 2**(b) shows the high-resolution spectrum of Bi 4*f* of the binary $BiOBr/Bi_4O_5Br_2$ composite. The binding energies of 159.2 and 164.5 eV were indexed to Bi $4f_{7/2}$ and Bi $4f_{5/2}$ peaks, respectively [20,23]. After being combined with $FeVO_4$, these doublet peaks shifted to the lower values of 158.7 and 164.0 eV, respectively. These Bi 4*f* signals further confirm that the oxidation state of the Bi element was +3 [20,23]. **Fig. 2**(c) shows Br 3*d* of $BiOBr/Bi_4O_5Br_2$ and $FeVO_4/Bi_4O_5Br_2/BiOBr$. For the binary $BiOBr/Bi_4O_5Br_2$ composite, two peaks at 68.4 and 69.2 eV corresponded to Br $3d_{5/2}$ and Br $3d_{3/2}$, respectively. For the ternary $FeVO_4/Bi_4O_5Br_2/BiOBr$ composite, these Br 3*d* peaks shifted to the lower binding energies of 67.9 and 68.9 eV. The presence of these Br 3*d* peaks signify that the Br element adopted the −1 oxidation state [20,23]. The high-resolution spectrum for Fe 2*p* in the ternary composite (**Fig. 2**(d)) revealed two main peaks of Fe $2p_{3/2}$ and Fe $2p_{1/2}$ (711.1 and 724.60 eV, respectively) which were located at higher binding energies than those of $FeVO_4$ (710.8 and 724.4 eV, respectively) [43–45]. The doublet signals of Fe 2*p* confirm the +3 oxidation state of Fe [43]. As is shown in **Fig. 2**(e), the splitting of V *2p* peaks in $FeVO_4$ was observed at binding energies of 517.7 and 524.7 eV, which were then assigned to the V $2p_{3/2}$ and V $2p_{1/2}$ states of the V^{5+} species [43,44]. However, two sub-peaks that corresponded to the V $2p_{3/2}$ and V $2p_{1/2}$ states of V with +4 oxidation state were observed at binding energies of 516.0 and 523.1 eV [46], wherein, the V^{4+} specie arose from certain oxygen vacancies [45]. These V 2*p* peaks shifted to the lower binding energies after $FeVO_4$ was introduced into the binary $BiOBr/Bi_4O_5Br_2$ heterostructure. **Fig. 2**(f) reveals that there were four O 1*s* peaks located at 529.6, 530.8, 532.1, and 533.2 eV implying four types of oxygen species exist in the ternary composite. Furthermore, these peaks were attributed to the chemical bonding of Bi−O [23], H−O in the adsorbed water on the material surface [45], V−O [45], and Fe−O [45], respectively. As can be seen from the high-resolution XPS spectrum of $FeVO_4/Bi_4O_5Br_2/BiOBr$ in comparison to $FeVO_4$ and $BiOBr/Bi_4O_5Br_2$, there are noticeable

shifts in the binding energies of the XPS peaks. Changes in the binding energy values resulted from the formation of a ternary heterostructure system suggesting the presence of a strong chemical interaction between these materials. This interaction could be beneficial for charge transfer between these materials and reduce the recombination of the photoactivated charge carriers [24,47,48].

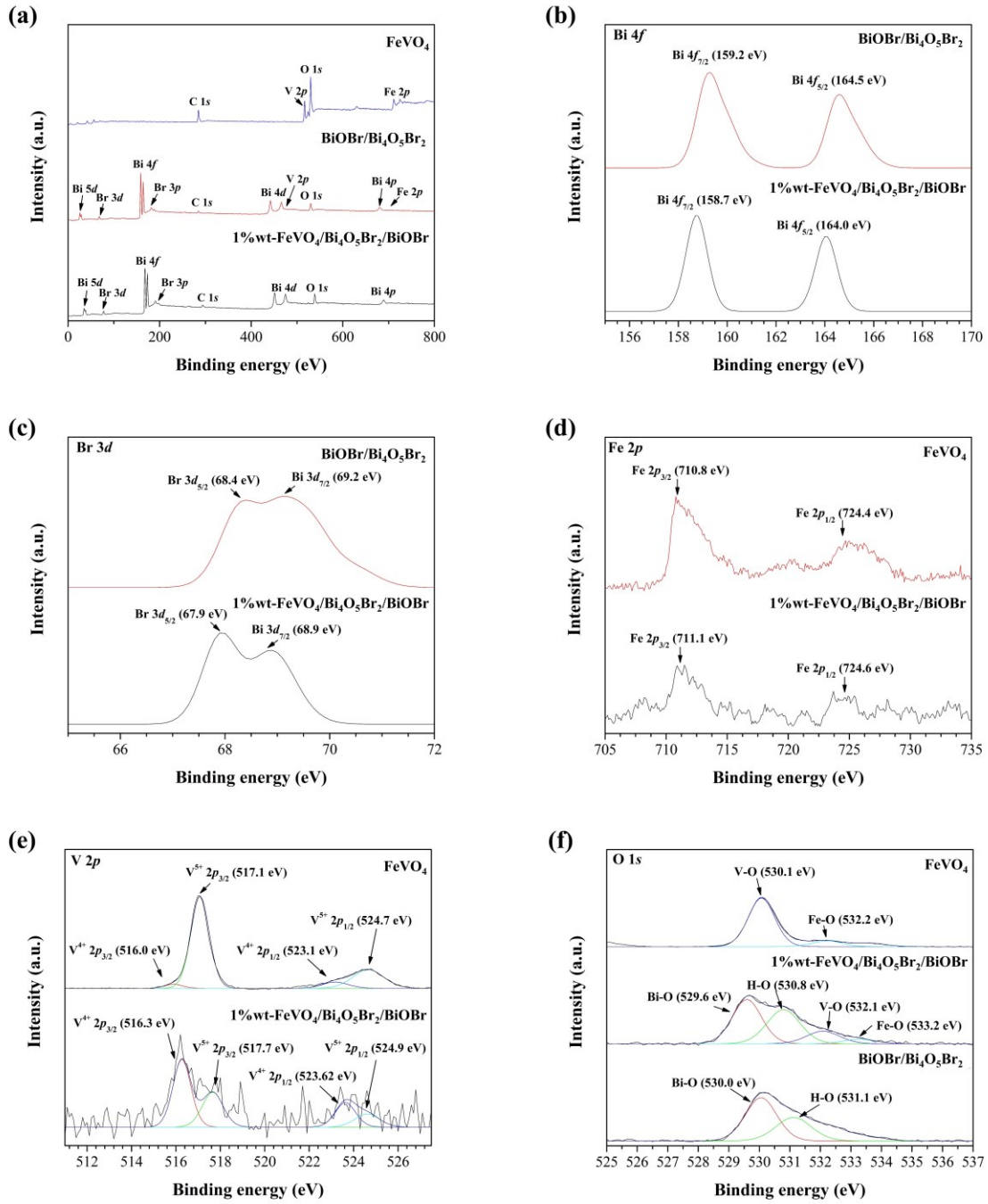

Fig. 2. XPS spectra of $FeVO_4$, $BiOBr/Bi_4O_5Br_2$ and 1%wt-$FeVO_4/Bi_4O_5Br_2/BiOBr$: (a) survey spectra and (b-f) high-resolution XPS spectra of Bi 4*f*, Br 2*p*, Fe 2*p*, V 2*p* and O 1*s*, respectively.

3.2. Morphological investigation

FESEM images of the BiOBr, $Bi_4O_5Br_2$, $FeVO_4$, $BiOBr/Bi_4O_5Br_2$, and 1%wt-$FeVO_4/Bi_4O_5Br_2/BiOBr$ powders are shown in **Fig. S1** and **Fig. 3**(a)-(c). FESEM (**Fig. S1**(a)) and TEM (**Fig. S2**(a)) images of BiOBr reveal a flower-like microsphere with an average diameter of 3.9 μm that is built up of ellipsoid-like nanoparticles with an average vertical height of 247 nm and an average width of 57 nm. EDS spectrum of BiOBr (**Fig. S1**(c)) presents the existence of Bi, O and Br elements with an atomic ratio of 1.10:1.01:1.00, respectively, which agrees with the stoichiometry of BiOBr. The FESEM (**Fig. S1**(b)) and TEM (**Fig. S2**(b)) images of $Bi_4O_5Br_2$ show a flower-like micro-spherical structure that is comprised of densely packed thin nanosheets. EDS spectrum of $Bi_4O_5Br_2$ (**Fig. S1**(d)) reveals the spectra of Bi, O and Br elements with a molar ratio of Bi:Br at 2.03 confirming the formation of a bismuth-rich compound. HRTEM images of BiOBr (inset of **Fig. S2**(a)) and $Bi_4O_5Br_2$ (inset of **Fig. S2**(b)) reveal the crystal lattice fringes with *d*-spacings of 0.197 and 0.198 nm, which corresponded to the (200) plane of tetragonal BiOBr and (422) plane of monoclinic $Bi_4O_5Br_2$, respectively. These findings confirm the crystalline structure of both materials.

For the binary $BiOBr/Bi_4O_5Br_2$ composite, flower-like microspheres with an average diameter of 3.8 μm were still observed (**Fig. 3**(a) and **Fig. S2**(c)). Morphologically, the flower-like micro-spherical structure is likely to be in a transitional phase between BiOBr and $Bi_4O_5Br_2$ as has been suggested by its moderately packed nanosheets. The combination of BiOBr and $Bi_4O_5Br_2$ in the binary composite was confirmed by HRTEM (**Fig. S2**(d)). The HRTEM image shows a distribution of nanoparticles with an average diameter of 13 nm on the

nanosheets. The nanoparticles revealed two lattice fringes of 0.279 and 0.359 nm that were consistent with the (110) and (101) planes of BiOBr. The nanoplate showed lattice intervals of 0.299 and 0.300 nm which corresponded to the $(41\bar{1})$ plane of $Bi_4O_5Br_2$. For $FeVO_4$, a large number of nanoparticles with an average diameter of about 100 nm were observed (**Fig. 3**(b)). FESEM (**Fig. 3**(c)) and TEM (**Fig. 4**(a)) images of the ternary 1%wt-$FeVO_4$/$Bi_4O_5Br_2$/BiOBr composite revealed that the $FeVO_4$ nanoparticles were anchored on the surface of the flower-like BiOBr/$Bi_4O_5Br_2$ microspheres. The corresponding EDS spectrum demonstrated the compositions of Fe, V, O, Bi, and Br elements (**Fig. 3**(d)). The actual weight percentages of $FeVO_4$ and BiOBr/$Bi_4O_5Br_2$ in the composite were calculated to be 0.98 and 98.91, respectively, which were close to those of the fabrication contents.

HRTEM image of the ternary 1%wt-$FeVO_4$/$Bi_4O_5Br_2$/BiOBr composite shown in **Fig. 4**(b) reveals lattice fringes with *d*-spacings of 0.356 and 0.170 nm which corresponded to the (120) and (514) planes of $FeVO_4$ and $Bi_4O_5Br_2$, respectively. HRTEM image presented in **Fig. 4**(c) reveals two sets of lattice fringes, for which the *d*-spacings of 0.164 and 0.160 nm could be assigned to the (114) and (212) planes of BiOBr, while the *d*-spacings of 0.365 and 0.366 nm belonged to the (112) plane of monoclinic $Bi_4O_5Br_2$. Additionally, HRTEM image presented in **Fig. 4**(d) reveals the lattice fringes of the $FeVO_4$, $Bi_4O_5Br_2$ and BiOBr phases in the ternary 1%wt-$FeVO_4$/$Bi_4O_5Br_2$/BiOBr composite indicating the formation of intimate contacts between these materials. Moreover, scanning TEM-EDS mapping on the ternary composite was recorded to obtain more information with regard to elemental distribution. As is shown in **Fig. 4**(e), the ternary composite composed of Fe, V, Bi, Br, and O elements that are homogeneously distributed in the ternary composite. These results clearly indicate the coexistence of $FeVO_4$ and BiOBr/$Bi_4O_5Br_2$, as well as an intimate contact between the component materials, confirming the presence of a ternary $FeVO_4$/$Bi_4O_5Br_2$/BiOBr heterojunction.

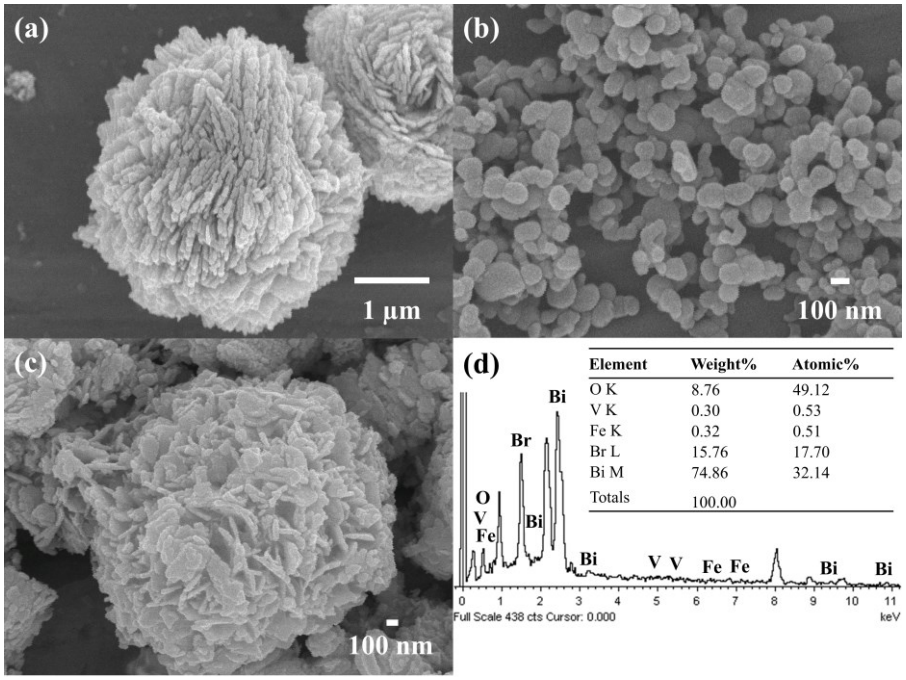

Fig. 3. FESEM images of (a) $BiOBr/Bi_4O_5Br_2$, (b) $FeVO_4$, and (c) 1%wt-$FeVO_4/Bi_4O_5Br_2/BiOBr$. (d) EDS spectrum with elemental compositions of 1%wt-$FeVO_4/Bi_4O_5Br_2/BiOBr$.

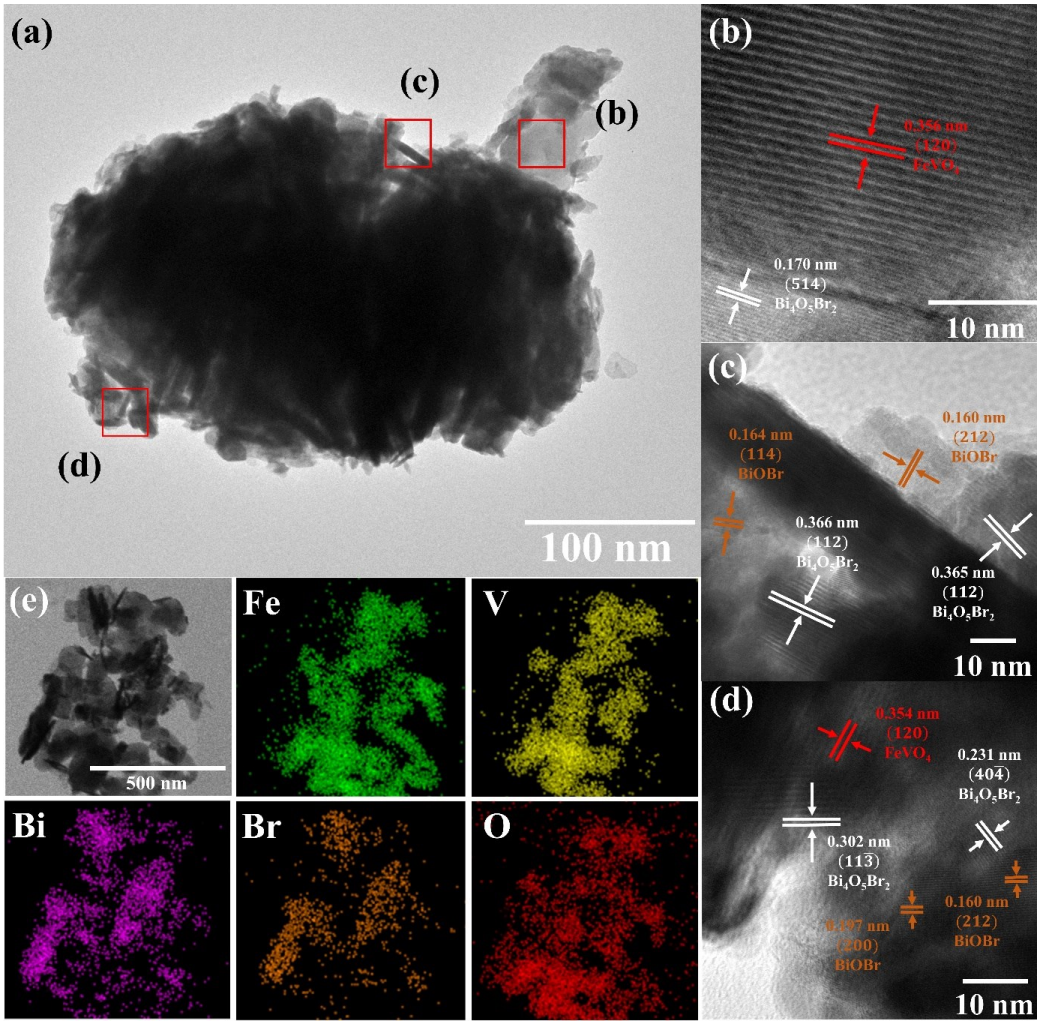

Fig. 4. (a) TEM image of the ternary 1%wt-$FeVO_4$/$Bi_4O_5Br_2$/BiOBr composite and (b-d) HRTEM images of $FeVO_4$ and BiOBr/$Bi_4O_5Br_2$ in the ternary composite. (e) Scanning TEM-EDS mapping of 1%wt-$FeVO_4$/$Bi_4O_5Br_2$/BiOBr.

3.3. Optical properties

Optical properties of $FeVO_4$, BiOBr, $Bi_4O_5Br_2$, BiOBr/$Bi_4O_5Br_2$, and 1%wt-$FeVO_4$/$Bi_4O_5Br_2$/BiOBr were investigated by UV-vis DRS analysis. The binary BiOBr/$Bi_4O_5Br_2$ heterojunction exhibited an absorption edge at around 480 nm (**Fig. 5**(a)), which was in between those of BiOBr (440 nm) and $Bi_4O_5Br_2$ (500 nm). The coupling of $FeVO_4$ with the binary BiOBr/$Bi_4O_5Br_2$ heterostructure relatively enhanced the absorption ability in the visible light region. In addition, an absorption edge of 1%wt-

$FeVO_4/Bi_4O_5Br_2/BiOBr$ was extended to a higher wavelength when compared to those of BiOBr, $Bi_4O_5Br_2$, and $BiOBr/Bi_4O_5Br_2$. The improved absorption capacity in the visible light region, after compositing $FeVO_4$ with $BiOBr/Bi_4O_5Br_2$, could improve the generation of charge carriers and consequently enhance photocatalytic activity. Moreover, the absorption spectrum of the ternary composite exhibited two absorption slopes at around 480 and 595 nm, which corresponded well with the absorption edges of the $BiOBr/Bi_4O_5Br_2$ and $FeVO_4$ parent materials. This indicated the coexistence of $FeVO_4$ and $BiOBr/Bi_4O_5Br_2$. The band gap energy (E_g) was determined from the Tauc equation [49] as follows;

$$\alpha h\nu = A(h\nu - Eg)^{n/2}$$

where α, h, ν, A, and E_g represent the absorption coefficient, Plank's constant, light frequency, constant, and the band gap energy of the materials, respectively. The n values depend upon characteristics of the optical transition of the semiconductor. For $FeVO_4$, BiOBr and $Bi_4O_5Br_2$, the n values were recorded at 4 for their indirect transition [20,50]. Thus, the corresponding E_g values of $FeVO_4$, BiOBr, and $Bi_4O_5Br_2$ were calculated to be 2.08, 2.93, and 2.60 eV, respectively.

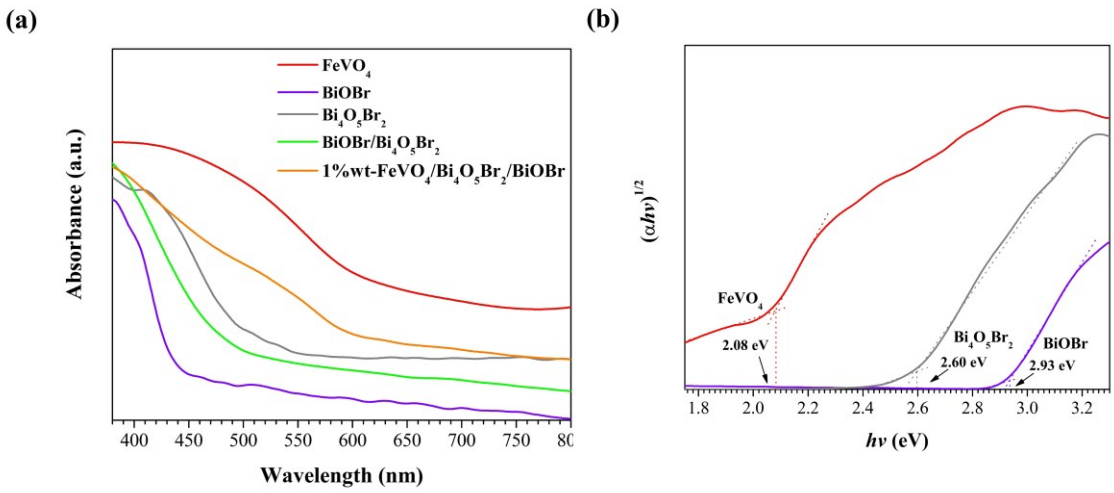

Fig. 5. (a) UV-vis DRS spectra of $FeVO_4$, BiOBr, $Bi_4O_5Br_2$, $BiOBr/Bi_4O_5Br_2$, and 1%wt-$FeVO_4/Bi_4O_5Br_2/BiOBr$. (b) Corresponding Tauc' plots of the single materials.

3.4. Photocatalytic degradation of organic pollutants

3.4.1. Effect of $FeVO_4$ content in ternary composites

Photocatalytic activities of the samples were evaluated by degrading RhB and MB dyes, as well as colorless SA under visible light irradiation. For the photolysis tests **(Fig. S3)**, the self-photodegradation of these organic compounds was negligible. **Fig. S3**(a) shows that BiOBr/$Bi_4O_5Br_2$ completely degraded RhB within 180 min, while BiOBr and $Bi_4O_5Br_2$ degraded 63.5% and 90.3% of RhB, respectively. Similarly, BiOBr/$Bi_4O_5Br_2$ exhibited higher %DE (66.9%) than did BiOBr (40.9%) and $Bi_4O_5Br_2$ (54.7%) towards MB within 360 min (**Fig. S3**(b). The BiOBr and $Bi_4O_5Br_2$ photocatalysts exhibited lower degrees of SA degradation with %DE of 22.7% and 30.5% relative to BiOBr/$Bi_4O_5Br_2$ (45.6%). The k_{app} values for the photodegradation of organic compounds by BiOBr/$Bi_4O_5Br_2$ were about 2.2 and 1.5 times higher than those of BiOBr and $Bi_4O_5Br_2$, respectively (**Fig. S3**(d)-(f)). These results imply the successfulness in the fabrication of binary BiOBr/$Bi_4O_5Br_2$ heterostructure which provided higher photocatalytic efficiencies than both BiOBr and $Bi_4O_5Br_2$.

Fig. S4(a)-(c) present the photocatalytic activities of $FeVO_4$, BiOBr/$Bi_4O_5Br_2$, and $FeVO_4$/$Bi_4O_5Br_2$/BiOBr with different $FeVO_4$ contents for the degradation of RhB, MB, and SA. The corresponding k_{app} values are presented in **Fig. S4**(d)-(f) and **Fig. S5**. As is shown in **Fig. S4**(a), there was almost no photodegradation of RhB in the presence of $FeVO_4$. On the other hand, the ternary $FeVO_4$/$Bi_4O_5Br_2$/BiOBr heterojunctions exhibited %DE of 93.2, 99.3, 88.9, 80.8 and 65.3 within 120 min with the $FeVO_4$ contents of 0.5, 1, 3, 6.25 and 12.5%wt, respectively. It was found that 1%wt-$FeVO_4$/$Bi_4O_5Br_2$/BiOBr exhibited the highest photocatalytic activity with a k_{app} value of 3.44×10^{-2} min^{-1} (**Fig. S4**(d)). Additionally, this ternary heterojunction exhibited the highest %DE (84.2% after 360 min) with a k_{app} value of 0.53×10^{-2} min^{-1} for the MB photodegradation among the other photocatalysts (**Figs. S4**(b) and (e)). Moreover, it exhibited improved photocatalytic efficiency and kinetic rate than those of

$FeVO_4$ and $BiOBr/Bi_4O_5Br_2$, which was attributed to increases in visible-light response and more efficient charge segregation and transportation at the heterostructure interfaces. In comparisons with our previous results [33,34], the k_{app} value for the RhB degradation by the ternary 1%wt-$FeVO_4/Bi_4O_5Br_2/BiOBr$ photocatalyst (3.44×10^{-2} min^{-1}) was around 2.6 and 1.6 times higher than for the binary 6.25%wt-$FeVO_4/Bi_7O_9I_3$ (1.30×10^{-2} min^{-1}) and 6.25%wt-$FeVO_4/BiOCl$ (2.15×10^{-2} min^{-1}) photocatalysts, respectively. Moreover, in this research, the photo-efficacy of $FeVO_4/Bi_4O_5Br_2/BiOBr$ was maximized after only small amounts of $FeVO_4$ (1%wt) was introduced into the host materials. These findings suggest that the ternary heterojunction could exhibit a significant performance by synergistic effect of the multicomponent, which then gave rise to the extension of the light absorption range and the efficient generation of the charge carriers.

We also tested the photocatalytic degradation of these dyes by using a commercial TiO_2 P25 photocatalyst (Degussa P25) under visible light irradiation. It is well known that P25 cannot be activated by visible light; however, in this work, 22.4% of RhB and 31.0% of MB were degraded in the presence of P25 within 120 min and 360 min of visible light irradiation, respectively. The degradation of these dyes in the presence of P25 could be attributed to the photosensitization effect of these dyes. For the photocatalytic degradation of dye, an indirect dye-sensitization process usually takes place in which the extra excited electrons from the lowest unoccupied molecular orbital (LUMO) of the dye molecules are injected into the conduction band of the semiconductor [51–53], facilitating the visible light sensitivity of P25 in the degradation of RhB and MB. Notably, RhB was significantly degraded by the ternary heterojunctions when compared to the degradation of MB. This could be attributed to more negative LUMO of RhB over that of MB which favored the transfer of the excited electrons from the LUMO of RhB molecules to the conduction band of the materials [54,55].

To further clarify the contribution of the dye-sensitization process, the photodegradation of colorless SA was also performed. **Figs. S4**(c) and (f) illustrate that P25 exhibited negligible photo-activity confirming that there was no occurrence of photosensitization process in the photocatalysis of colorless SA [56]. Introducing 1%wt of $FeVO_4$ into the binary $BiOBr/Bi_4O_5Br_2$ heterojunction could maximize the photocatalytic activity of the ternary $FeVO_4/Bi_4O_5Br_2/BiOBr$ heterojunction, where 12.5, 45.6 and 57.2% of SA were degraded by $FeVO_4$, $BiOBr/Bi_4O_5Br_2$ and 1%wt-$FeVO_4/Bi_4O_5Br_2/BiOBr$, respectively.

It should be noted that the loading amount of $FeVO_4$ strongly affected the photocatalytic activity. Further increases in $FeVO_4$ content led to a decrease in both %DE and k_{app}. This could be ascribed to an excess amount of $FeVO_4$ nanoparticles, which may induce agglomeration and cover the active surface of the flower-like $BiOBr/Bi_4O_5Br_2$ microstructures. These phenomena resulted in the poor utilization of light, and thus a reduction in a generation of electron-hole pairs [47,57,58]. The photocatalytic activity of the physical mixture of 1%wt of $FeVO_4$ and $BiOBr/Bi_4O_5Br_2$ (denoted as PM) was also tested. The results indicate that it provided lower %DE for RhB (91.9%,120 min), MB (52.3%, 360 min), and SA (26.3%, 360 min) than those of $BiOBr/Bi_4O_5Br_2$ and 1%wt-$FeVO_4/Bi_4O_5Br_2/BiOBr$. The results further indicate that the formation of the ternary heterojunction by coupling $FeVO_4$ with binary $BiOBr/Bi_4O_5Br_2$ heterojunction could be responsible for the enhanced photocatalytic activity rather than the physically mixing of these materials.

As reusability is an important factor for practical usages, RhB photodegradation by the binary and ternary heterojunction photocatalysts were carried out in three-successive runs. As is shown in **Fig. S6**, 1%wt-$FeVO_4/Bi_4O_5Br_2/BiOBr$ exhibited no significant changes in the photodegradation of RhB after three recycle reactions. However, a loss in photocatalytic efficiency of RhB was detected for the binary $BiOBr/Bi_4O_5Br_2$ photocatalyst. This could have

arisen from the unremovable adsorbed RhB molecules on the photocatalyst's surface, lowering the surface-active site of BiOBr/$Bi_4O_5Br_2$. Furthermore, it could have occurred because of the reduction of Bi^{3+} by photoactivated electrons since the reduction potential of Bi(III)/Bi (0.308 V *vs.* NHE) is more positive than either CB of BiOBr (-0.032 V *vs.* NHE) or $Bi_4O_5Br_2$ (-0.15 V *vs.* NHE) [59].

3.4.2. Effects of photocatalytic conditions on RhB degradation

A series of photocatalytic experiments were carried out to evaluate the effects of RhB initial concentration and photocatalyst dosage on RhB degradation, the results of which are shown in **Figs. S7** and **S8**. At constant amounts of the photocatalyst (100 mg of 1%wt-$FeVO_4$/$Bi_4O_5Br_2$/BiOBr), an increase in RhB concentration from 10 to 40 ppm led to a decrease in the photocatalytic efficiency and degradation rate (**Fig. S7**(a) and (c)). These results may have occurred because the reaction solution became more intensely colored as the initial dye concentration was increased, shielding the light penetration to the photocatalyst's surface [33,57]. Consequently, the generation of electron-hole pairs was decreased, limiting the production of the active species that are responsible for photodegradation.

In the experiments, the photocatalyst dosage was varied from 50 to 250 mg and was administered along with an RhB initial concentration of 10 ppm. RhB degradation increased along with increases in the photocatalyst dosage at up to 200 mg (**Figs. S7**(b) and (d)). The increase in RhB degradation could have been due to an increase in the available active sites on the photocatalyst's surface. However, RhB degradation declined when 250 mg of photocatalyst was used. This occurred because excessive amounts of the photocatalyst suspended in the solution scattered the incident light, while the light penetration through the solution was diminished. Consequently, there was a reduction in the number of active species produced during the photocatalytic reaction [33,57].

3.5. Photocatalytic Cr(VI) reduction and optimization of photocatalytic conditions

To study the feasibility of utilizing the ternary 1%wt-$FeVO_4/Bi_4O_5Br_2/BiOBr$ heterojunction for photocatalytic reduction, 20 ppm of the Cr(VI) aqueous solution was used as a studied target. As is shown in **Fig. 6**(a), both P25 and $FeVO_4$ exhibited almost no photocatalytic Cr(VI) photoreduction, whereas $BiOBr/Bi_4O_5Br_2$ reduced approximately 90% of Cr(VI). The 1%wt-$FeVO_4/Bi_4O_5Br_2/BiOBr$ photocatalyst exhibited the highest photoreduction efficiency (%RE = 99.1) and the photoreduction rate was 2 times faster than that of $BiOBr/Bi_4O_5Br_2$. In addition, the kinetic rates (**Fig. 6**(b) and **Fig. S9**(a)) are in a good agreement with the photoreduction efficiencies.

The photoreduction efficiency of the Cr(VI) solution with a higher initial concentration (30 ppm) by 1%wt-$FeVO_4/Bi_4O_5Br_2/BiOBr$ was further tested. As is shown in **Fig. 6**(a), although 1%wt-$FeVO_4/Bi_4O_5Br_2/BiOBr$ was capable of degrading only 33.9% of Cr(VI), it still provided higher efficiency than those of $FeVO_4$ (%RE = 2.5) and $BiOBr/Bi_4O_5Br_2$ (%RE = 25.2). The initial pH of the 30 ppm Cr(VI) solution was then adjusted from 6 (initial pH) to 3, 5, 7 and 9 in attempts to improve photoreduction activity, the results for which are shown in **Fig. 6**(c) and (d). Photoreduction was significantly improved with %RE of 72.3 and 47.1 at pH values of 3 and 5, and k_{app} of 0.66×10^{-2} and 0.43×10^{-2} min^{-1}, respectively. On the basis of the thermodynamic aspect, Cr(VI) ions exist in different ionic forms under different pH conditions. Under acidic condition, Cr(VI) ions in the $HCrO_4^-$ and $Cr_2O_7^{2-}$ forms are the dominant species, while CrO_4^{2-} is a dominant species under neutral and basic conditions [60,61]. The reduction potentials of the $HCrO_4^-/Cr^{3+}$ couple (1.35 V *vs*. NHE) and the $Cr_2O_7^{2-}/Cr^{3+}$ couple (1.33 V *vs*. NHE) are more positive than that of the $CrO_4^{2-}/Cr(OH)_3$ couple (-0.13 V *vs*. NHE) [62]. As a result, the reduction of Cr(VI) to Cr(III) ions in the acidic solution became easier than in the neutral and basic solutions. Additionally, in the basic solution, the $Cr(OH)_3$ produced from the

reduction of Cr(VI) in the CrO_4^{2-} form could adsorb and block the active sites of the photocatalyst, decreasing the photocatalytic activity [63,64].

Additionally, we also studied the effect of photocatalyst dosage on the Cr(VI) photoreduction. The reaction was carried out by fixing the Cr(VI) concentration at 30 ppm along with the initial pH value. **Fig. 6**(e) and (f) clearly show that an increase in the photocatalyst dosage from 50 to 200 mg significantly improved the Cr(VI) photoreduction efficiency and rate; %RE and k_{app} were distinctly enhanced to 96.0 and 2.07×10^{-2} min^{-1} when using 200 mg of the photocatalyst. This outcome resulted by an increase in the active sites on the photocatalyst's surface, wherein the generation of the active species involved in the photocatalytic reaction increased. Notably, the effects of the solution's opacity and light scattering occurred as a result of using large amounts of suspended photocatalyst powder on the photocatalytic activity, which did not take place in the event of the Cr(VI) reduction. This could have occurred because the color of the Cr(VI) solution was relatively transparent when compared to that of the RhB solution.

Subsequently, we cross-studied the effects of the solution pH and photocatalyst dosage in order to maximize the photocatalytic activity of the photocatalyst for a reduction of 30 ppm Cr(VI). We investigated Cr(VI) reduction at the solution pH of 3 using different amounts of the ternary 1%wt-$FeVO_4/Bi_4O_5Br_2/BiOBr$ photocatalyst (50 to 200 mg). As is shown in **Fig. 6**(g), by using 200 mg of the photocatalyst, %RE was around 96.2 which was nearly identical to what we recorded when similar amounts of the photocatalyst were used without adjusting pH (**Fig. 6**(e)). However, by considering the k_{app} values for these two conditions, Cr(VI) photoreduction in the acidic environment ($k_{app} = 2.29 \times 10^{-2}$ min^{-1}) (**Fig. 6**(h)) was higher than when the solution pH was not adjusted ($k_{app} = 2.07 \times 10^{-2}$ min^{-1}) (**Fig. 6**(f)). Therefore, under the study conditions, it can be concluded that the photocatalytic Cr(VI) reduction activity could be maximized by using 200 mg of the photocatalyst and decreasing the solution pH to 3.

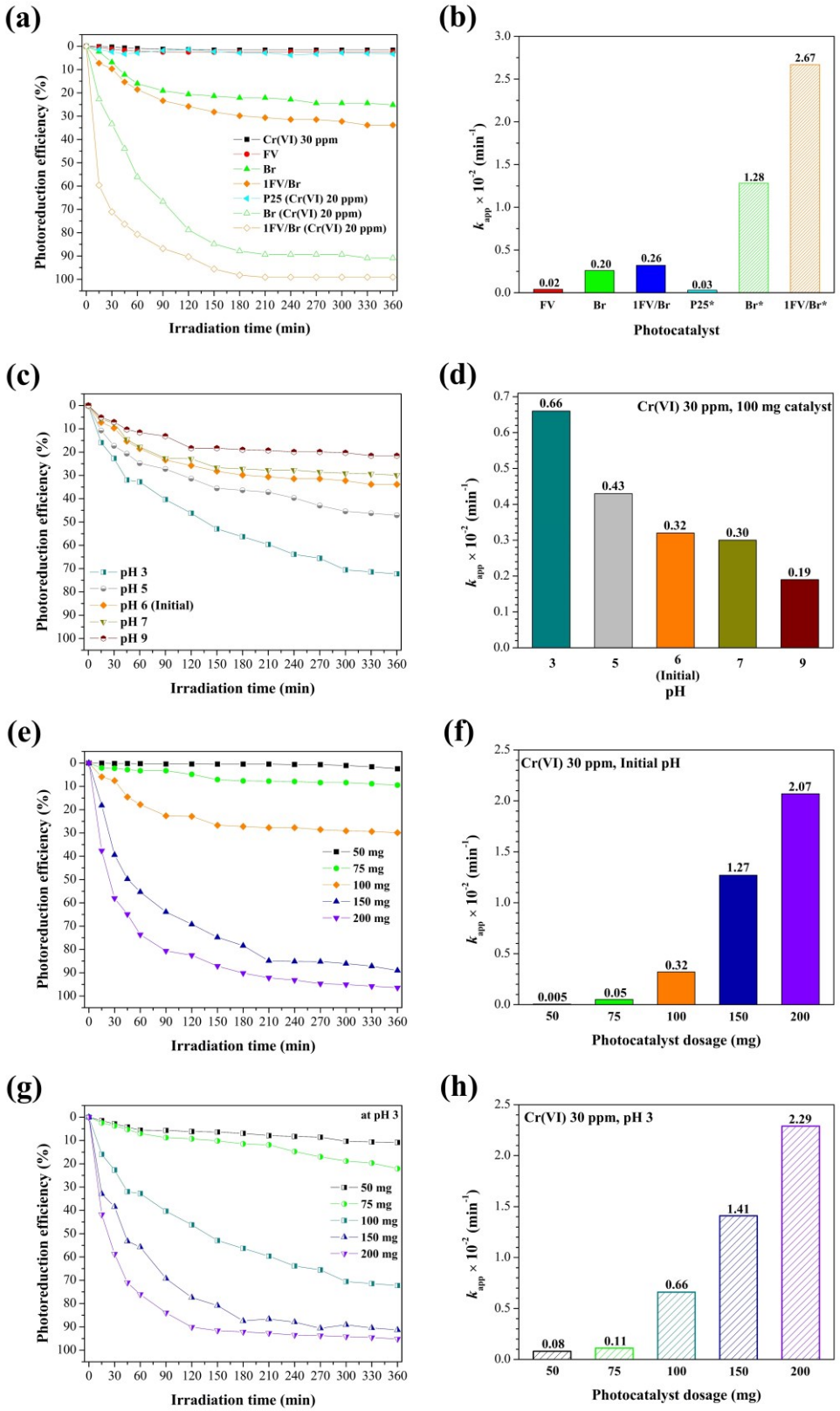

Fig. 6. (a-b) Effect of initial Cr(VI) concentration (20 ppm (signified with *) and 30 ppm) on photoreduction activity of the selected photocatalysts. Photoreduction efficiency and the corresponding kinetic rate of the ternary 1%wt-$FeVO_4/Bi_4O_5Br_2/BiOBr$ photocatalyst were

affected by (c-d) the solution pH and photocatalyst dosage at (e-f) both the initial pH and (g-h) pH 3 when using 30 ppm of Cr(VI).

3.6. Simultaneous photocatalytic removal of Cr(VI) and RhB by $FeVO_4/Bi_4O_5Br_2/BiOBr$ in combined pollution system

Since dyes and heavy metal ions often co-exist in wastewater, the simultaneous removal effect of the Cr(VI) and RhB co-exist system in visible light-irradiated 1%wt-$FeVO_4/Bi_4O_5Br_2/BiOBr$ photocatalyst was investigated. By fixing the initial Cr(VI) concentration (30 ppm) and photocatalyst dosage (100 mg), the concentration of the co-existing RhB was varied (5, 10 and 20 ppm) to investigate the photo-efficacy of this ternary photocatalyst in the Cr(VI)/RhB combined pollution system. The results presented in **Figs. 7** and **S10. Fig. 7**(a) clearly shows that, in the presence of RhB, the photoreduction efficiency of Cr(VI) was significantly promoted. The %RE increased from 33.9 to 37.5, 54.8 and 61.9 after adding 5, 10 and 20 ppm of RhB, respectively. Under these circumstances, 41.2, 39.6, and 14.3% of RhB were also simultaneously degraded (**Fig. 7**(b)). RhB degradation was remarkably decreased by 25.3% after the RhB concentration was increased from 10 to 20 ppm. On the contrary, the photoreduction efficiency of Cr(VI) increased only by 7.1%. Additionally, the k_{app} values for Cr(VI) reduction (**Fig. 7**(c)) were 0.56×10^{-2} and 0.65×10^{-2} min^{-1} for the combined systems at 10 and 20 ppm RhB, respectively. In these systems, the k_{app} values (**Fig. 7**(d)) for RhB degradation were 0.20×10^{-2} and 0.06×10^{-2} min^{-1}. By considering the photoreduction of Cr(VI) and the photodegradation of RhB along with the k_{app} values, we decided that an introduction of 10 ppm of RhB into the combined system would be sufficient to greatly improve the photoreduction efficiency of Cr(VI) with a moderate RhB degradation efficiency.

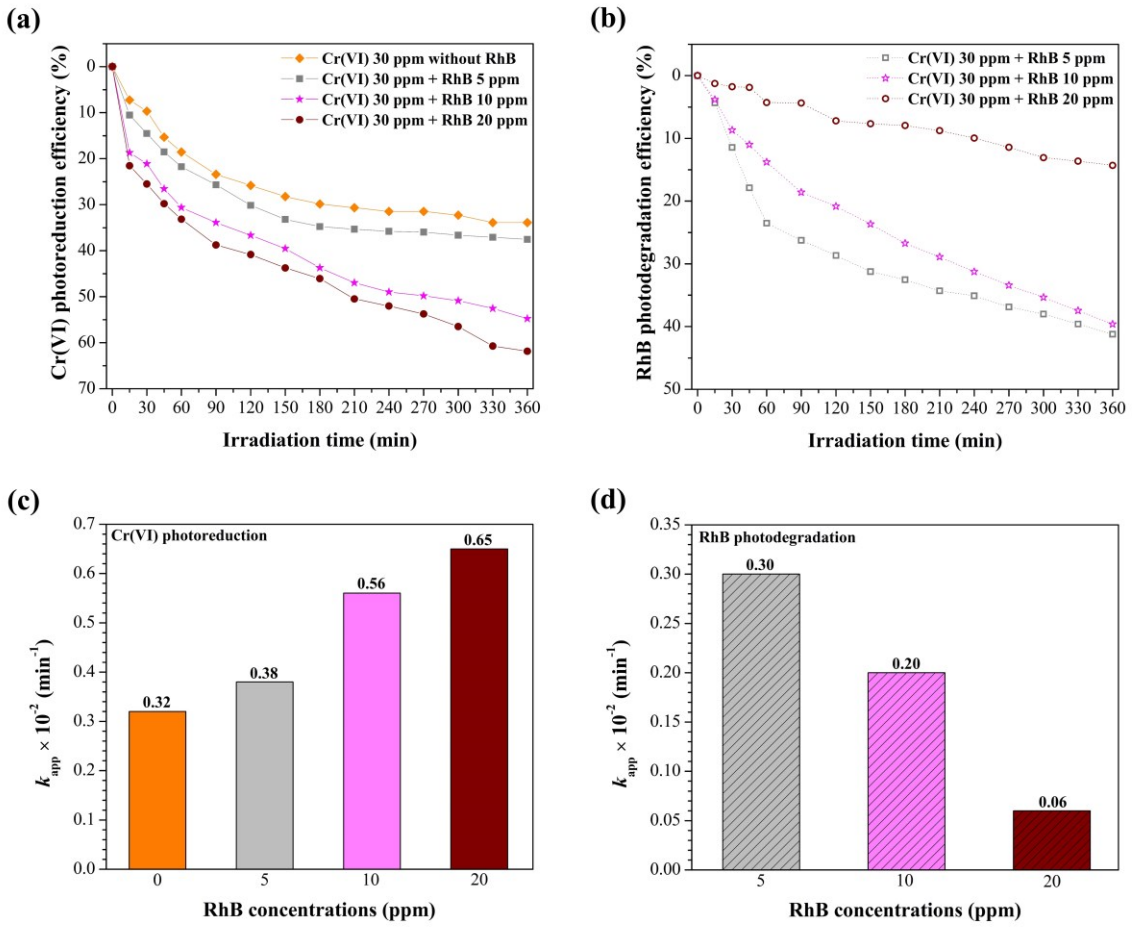

Fig. 7. (a) Photoreduction of Cr(VI) and (b) photodegradation of RhB in the Cr(VI) and RhB co-exist system over the ternary 1%wt-$FeVO_4/Bi_4O_5Br_2/BiOBr$ photocatalyst; the corresponding k_{app} values for (c) Cr(VI) photoreduction and (d) RhB photodegradation.

As has been expressed in the previous section, the photoreduction Cr(VI) activity could be maximized by adjusting the pH of the solution to 3 and/or by increasing the photocatalyst dosage to 200 mg (**Fig. 6**). Thereby, we adjusted the pH value of the mixed Cr(VI) (30 ppm) and RhB (10 ppm) solution to 3 and/or employed 200 mg of the ternary photocatalyst with the aim of achieving the highest photoreduction Cr(VI) activity. The Cr(VI) photoreduction and RhB photodegradation efficiencies, along with the corresponding k_{app} values are summarized in **Table S1**. As can be seen in **Fig. 8**(a) and (c), at the initial pH of the mixed solution, the Cr(VI) photoreduction efficiencies increased from 54.8 to 99.7% when using 100 and 200 mg

of the photocatalyst, respectively, within 360 min. Similarly, at a pH value of 3 in the mixed solution, with the use of 200 mg of the photocatalyst, the Cr(VI) reduction efficiency also increased to 99.8%. Although, the Cr(VI) photoreduction efficiency for the latter condition was comparable to that of the former condition, the kinetic rate was relatively faster (k_{app} = 4.53×10^{-2} min^{-1} at pH of 3, and 2.73×10^{-2} min^{-1} at the initial pH) (**Fig. 8**(c)). These results suggest that, under the latter condition, the photocatalyst was more effective in reducing Cr(VI) in the combined pollutant system. Under this condition, Cr(VI) was completely reduced within 150 min of irradiation, while 98.2% of RhB was degraded within 360 min of irradiation (**Fig. 8**(b)). These results indicate that the presence of RhB in the combined pollutant system can lead to an increment of photoreduction of Cr(VI) implying that RhB acts as an efficient photosensitizer for the Cr(VI) reduction process. **Fig. S11** presents the photocatalytic data with error bars that are based on the standard deviations of three parallel experiments. The small standard deviation for each irradiated time interval reflects the accuracy of the sample data.

As is understood, the adsorption of dye molecules on a photocatalyst's surface is required in a dye-sensitization process in order to inject electrons from LUMO of the excited dye molecules to a conduction band of a semiconductor [35]. Typically, RhB exists in two forms in an aqueous medium, the cationic (RhB^{+}) and zwitterion ($RhB^{\pm}$) forms, depending upon the pH of the solution. The cationic form exists at pH values lower than the pKa of RhB (3.7), while the zwitterion form exits at pH values higher than the pKa due to a deprotonation of its carboxyl group [65]. Therefore, to elucidate the adsorption ability toward RhB molecules, zeta potentials of 1%wt-$FeVO_4/Bi_4O_5Br_2/BiOBr$ were measured at different pH values of the solution. **Fig. S12** indicates that the zeta potentials varied from -12.8 to -22.4 mV. Thus, at a pH value beyond 2, the photocatalyst's surface charge is negatively charged. As a result, it could well adsorb RhB molecules in both forms via an electrostatic interaction, and consequently, fulfill the dye-sensitization requirement.

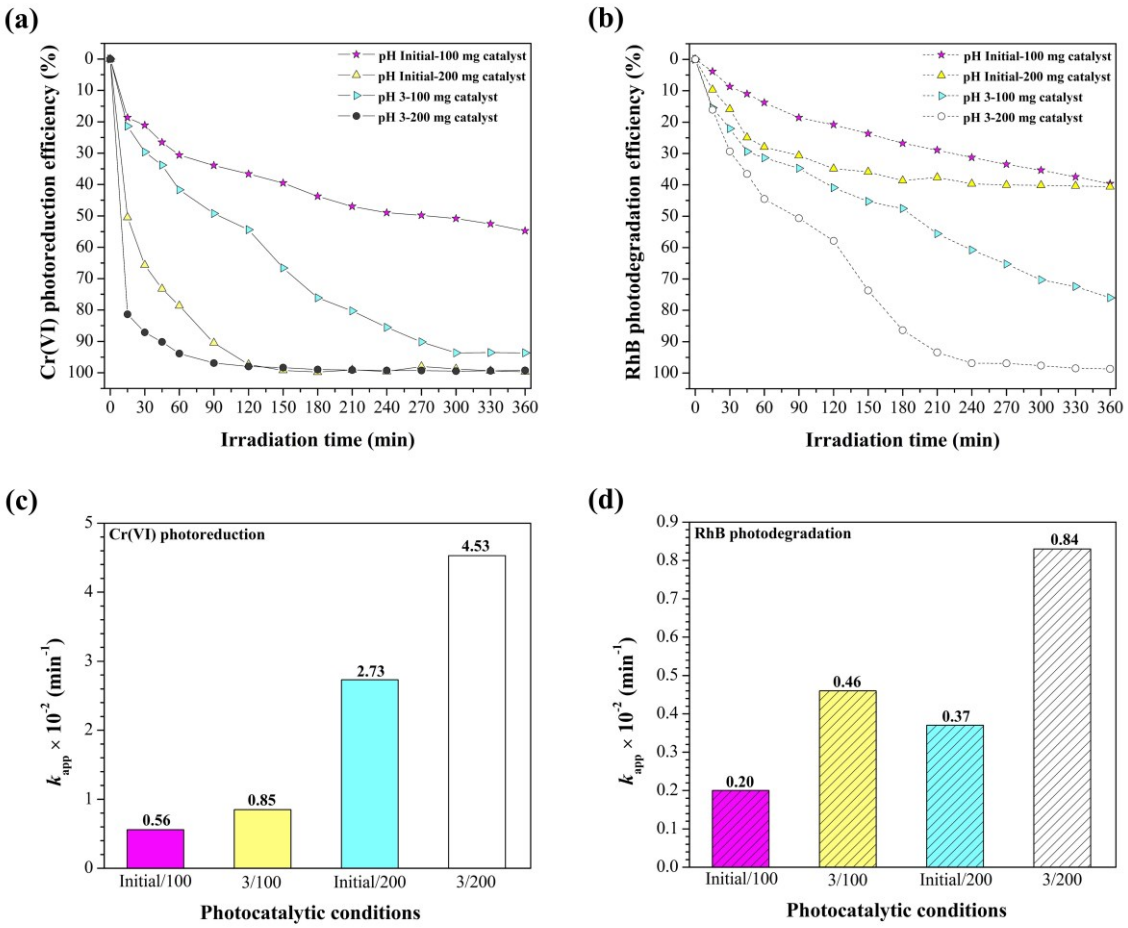

Fig. 8. (a) Photoreduction of Cr(VI) and (b) photodegradation of RhB in the coexistence over the 1%wt-$FeVO_4/Bi_4O_5Br_2/BiOBr$ photocatalyst influenced by pH value and photocatalyst dosage; corresponding k_{app} values for (c) Cr(VI) photoreduction and (d) RhB photodegradation.

To further clarify this point, an anionic dye (methyl orange, MO) was introduced into the combined pollution system instead of RhB. **Fig. S13**(a) shows that, in the Cr(VI)/MO combined system, Cr(VI) photoreduction was significantly suppressed. In terms of the adsorption ability, 21% of the RhB molecules were adsorbed by the 1%wt-$FeVO_4/Bi_4O_5Br_2/BiOBr$ photocatalyst, whereas only 4% of MO were adsorbed. Therefore, the requirements of the dye-sensitization mechanism could not be fulfilled by MO. It should be noted that the adsorption percentages of Cr(VI) remain fairly constant by approximately 10% in both systems. Moreover, the Cr(VI) photoreduction efficiency in the Cr(VI)/MO combined

system was significantly lower than that of the Cr(VI) single pollutant system although the levels of adsorption of Cr(VI) in these systems were similar. Remarkably, in the MO single system, 60% and 32.7% of MO molecules were adsorbed and degraded by the ternary photocatalyst, respectively, which were much higher than those of the Cr(VI)/MO combined system (**Fig. S13**(b)). A lowering in the adsorption and degradation abilities towards MO and the reduction ability of Cr(VI) in the coexistence could be elucidated by considering the UV–vis absorption spectra of the Cr(VI) solution, along with the mixed solution of Cr(VI) and MO remained after the photocatalytic process. As is shown in **Fig. S13**(d), λ_{max} of Cr(VI) in the mixed Cr(VI) and MO solutions shifted from 352 nm to 374 nm. On the other hand, the shift in λ_{max} was not observed in the case of RhB (**Fig. S13**(c)). This finding implies that the presence of MO in the combined system could induce the formation of a Cr(VI)-MO complex, consequently decreasing free Cr(VI) ions and MO molecules that are available for the photocatalytic reaction.

In addition to the MO dye, SA was introduced to the combined pollution system instead of RhB. **Fig. S14**(a) shows that 5 ppm of SA did not improve Cr(VI) photoreduction, which could be ascribed to the competitive adsorption of SA (34.5%). However, a slight incremental increase in the Cr(VI) photoreduction efficiency to 40% was observed by adding 10 ppm of SA. Despite the lack of sensitization ability of SA, it could act as a hole scavenger which consequently reduced electron-hole pair recombination, and thus, facilitated Cr(VI) photoreduction efficiency. However, the incremental increase in the Cr(VI) photo-efficiency by SA in the Cr(VI)/SA combined system was not as significant as it was for RhB, suggesting the significance of the dye-sensitization mechanism that was induced by the RhB molecules.

The reusability of the ternary photocatalyst for the photoreduction of Cr(VI) (20 ppm) over the binary and ternary heterojunction photocatalysts were evaluated. As is shown in **Fig. 9**(a), the ternary 1%wt-$FeVO_4/Bi_4O_5Br_2/BiOBr$ photocatalyst maintained high photoreduction

efficiency towards Cr(VI) without a significant decrease in photo-efficiency after three successive runs, while the binary $BiOBr/Bi_4O_5Br_2$ photocatalyst exhibited a significant loss in photo-efficiency. The loss in recyclability of the binary photocatalyst could be arisen from unremovable adsorbed Cr(VI) ions on its surface, and the reduction of Bi^{3+} ions by photoactivated electrons as has been discussed in the previous section. Similarly, the reusability and stability of the ternary heterojunction photocatalyst for the photocatalytic removal of Cr(VI) and RhB in the Cr(VI)/RhB combined pollutant system were also investigated under conditions including 30 ppm Cr(VI)/10 ppm RhB, solution pH of 3, and 200 mg of the photocatalyst. As is shown in **Fig. 9**(b), 1%wt-$FeVO_4/Bi_4O_5Br_2/BiOBr$ exhibited no significant changes in the removal of RhB and Cr(VI) after the three-recycling test. The XRD patterns (**Fig. 9**(c)) and FESEM image (**Fig. 9**(d)) indicate that 1%wt-$FeVO_4/Bi_4O_5Br_2/BiOBr$ maintained its crystalline structure and three-dimensional flower-like structure. Moreover, as was determined by ICP-OES analysis, Fe and V ions were not detected in the supernatant solution. These results prove that the ternary heterojunction photocatalyst is reusable and stable against photocorrosion and chemical corrosion. Its reusability and stability towards Cr(VI) reduction and RhB degradation were probably due to the migration of photoactivated electrons from the binary $BiOBr/Bi_4O_5Br_2$ heterojunction to $FeVO_4$ through the intimate interfacial contact between $BiOBr/Bi_4O_5Br_2$ and $FeVO_4$. This could be beneficial in preventing the reduction of Bi^{3+} ions in the ternary heterojunction. The photocatalytic removal of Cr(VI) and RhB in the coexisting system by 1%wt-$FeVO_4/Bi_4O_5Br_2/BiOBr$, when compared with the outcomes of previously published reports, are summarized and shown in **Table S2**. Differences in the efficiency could have been caused by variations in the photocatalytic conditions such as type and power of the light source, pH solution, catalyst dosage, and type of catalyst. However, the ternary 1%wt-$FeVO_4/Bi_4O_5Br_2/BiOBr$ photocatalyst exhibited better photo-activity under the same photocatalytic conditions than that of the single and binary photocatalysts, P25, and

even the counterpart photocatalysts (6.25%wt-$FeVO_4/Bi_7O_9I_3$ [33] and 6.25%wt-$FeVO_4$/BiOCl [34]).

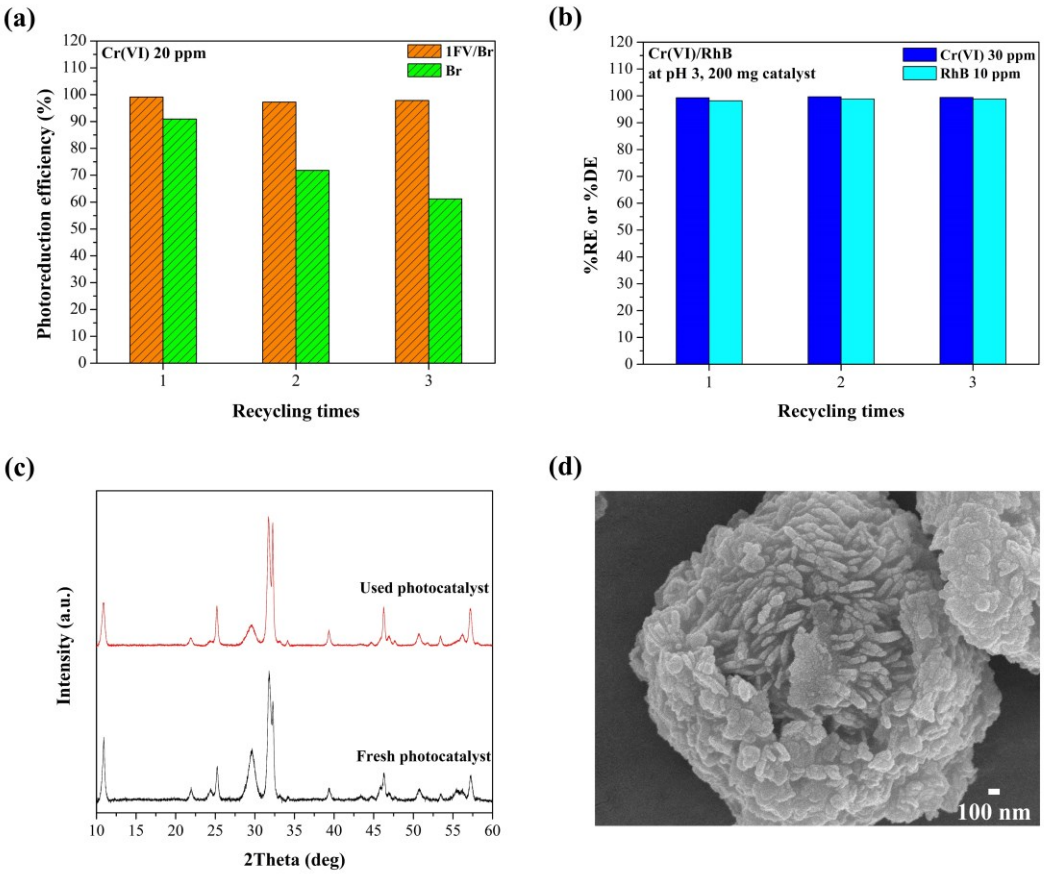

Fig. 9. Cyclic runs of (a) photoreduction of 20 ppm Cr(VI) in a single pollutant system over BiOBr/$Bi_4O_5Br_2$ (Br) and 1%wt-$FeVO_4/Bi_4O_5Br_2$/BiOBr (1FV/Br) samples, (b) photodegradation of RhB and photoreduction of Cr(VI) in the Cr(VI)/RhB combined pollution system under conditions including 30 ppm Cr(VI)/10 ppm RhB, solution pH of 3, and 200 mg of photocatalyst over 1%wt-$FeVO_4/Bi_4O_5Br_2$/BiOBr. (c) XRD patterns before and after recycling experiments towards Cr(VI) and (d) the corresponding FESEM image of 1%wt-$FeVO_4/Bi_4O_5Br_2$/BiOBr after the three-recycling test.

3.7. Discussion on enhanced photocatalytic activity

The charge carrier separation properties of the heterojunction photocatalysts in comparison to the single photocatalysts were determined by PL. Generally, a PL emission

signal arises from the recombination of charge carriers in a semiconductor. A lower PL emission intensity indicates a lower electron-hole pair recombination which facilitates a photocatalytic reaction [66]. The PL spectra of BiOBr, $Bi_4O_5Br_2$, BiOBr/$Bi_4O_5Br_2$ and 1%wt-$FeVO_4$/$Bi_4O_5Br_2$/BiOBr are presented in **Fig. 10**(a). It can be seen that 1%wt-$FeVO_4$/$Bi_4O_5Br_2$/BiOBr emitted the lowest PL emission intensity in comparison to the single BiOBr and $Bi_4O_5Br_2$, and binary BiOBr/$Bi_4O_5Br_2$ materials. This result suggests that the fabrication of the ternary heterojunction can effectively reduce electron-hole recombination, which is essential in the enhancement of photocatalytic activity.

EIS was used to determine the charge transfer resistance of the materials [66,67]. A smaller arc radius in the EIS Nyquist plot indicated a lower charge transfer resistance at the interface between the electrode and the electrolyte solution, implying a better migration of the charge carrier. As is shown in **Fig. 10**(b), the arc radius of the ternary 1%wt-$FeVO_4$/$Bi_4O_5Br_2$/BiOBr electrode exhibited the smallest among the single and binary electrodes. This result implies the highest level of effective charge transfer efficiency, and therefore, a large number of charge carriers took part in the photocatalytic reactions [67–69]. The arc radius of this electrode was also smaller than that of the physical mixture electrode, implying that the ternary 1%wt-$FeVO_4$/$Bi_4O_5Br_2$/BiOBr heterostructure was formed by a chemically interaction. Moreover, the arc radius of the physical mixture electrode was larger than that of the binary BiOBr/$Bi_4O_5Br_2$ electrode, signifying the successfulness in the formation of the ternary heterostructure. The 1%wt-$FeVO_4$/$Bi_4O_5Br_2$/BiOBr/RhB film on the FTO glass was also fabricated and then analyzed to clarify the sensitization role of RhB in the enhancement of the photocatalytic activity. The arc radius of the 1%wt-$FeVO_4$/$Bi_4O_5Br_2$/BiOBr/RhB film was significantly smaller than that of 1%wt-$FeVO_4$/$Bi_4O_5Br_2$/BiOBr, confirming that RhB indeed promoted the transportation of charge

carriers in the ternary 1%wt-$FeVO_4/Bi_4O_5Br_2/BiOBr$ system [70], which resulted in remarkably enhanced photocatalytic activity.

Fig. 10(c) shows the transient photocurrent responses of the $FeVO_4$, BiOBr, $Bi_4O_5Br_2$, $BiOBr/Bi_4O_5Br_2$, 1%wt-$FeVO_4/Bi_4O_5Br_2/BiOBr$ and physical mixture electrodes. The photocurrent responses of the $BiOBr/Bi_4O_5Br_2$ and 1%wt-$FeVO_4/Bi_4O_5Br_2/BiOBr$ electrodes were enhanced by comparison with that of the other electrodes. The 1%wt-$FeVO_4/Bi_4O_5Br_2/BiOBr$ electrode exhibited the largest photocurrent density, indicating that it had a high ability to generate and transfer photoactivated charge carriers. In combining the PL, EIS, and photocurrent responses results, the interfacial charge transfer efficiency in 1%wt-$FeVO_4/Bi_4O_5Br_2/BiOBr$ was greatly enhanced when compared with $BiOBr/Bi_4O_5Br_2$, which is occurred as a result of the formation of multi-heterojunctions.

The N_2 adsorption-desorption isotherms and pore size distributions of the $FeVO_4$, $BiOBr/Bi_4O_5Br_2$, and 1%wt-$FeVO_4/Bi_4O_5Br_2/BiOBr$ samples are shown in **Fig. S15**. The $BiOBr/Bi_4O_5Br_2$ and 1%wt-$FeVO_4/Bi_4O_5Br_2/BiOBr$ samples exhibited type-IV isotherms with the hysteresis loops in the range of 0.45-1.0 P/P_0, which is known to be a characteristic of slit-like mesopores that are formed by plate-like particles [26]. In addition, the pore size distribution curves reveal that the $BiOBr/Bi_4O_5Br_2$ and 1%wt-$FeVO_4/Bi_4O_5Br_2/BiOBr$ had mesopores with pore diameters in the range of 18–22 nm and the pore volume of the $BiOBr/Bi_4O_5Br_2$ was the highest. The BET surface area of $FeVO_4$, $BiOBr/Bi_4O_5Br_2$ and 1%wt-$FeVO_4/Bi_4O_5Br_2/BiOBr$ were 19.8, 46.8, and 42.3 m^2g^{-1} with total pore volumes of 0.0415, 0.3340, and 0.2367 cm^3g^{-1}, respectively. The slightly decreases in the surface area and total pore volume of 1%wt-$FeVO_4/Bi_4O_5Br_2/BiOBr$ could be due to the deposition of $FeVO_4$ nanoparticles on the $BiOBr/Bi_4O_5Br_2$ surface, decreasing the number of cavities on the surface of $BiOBr/Bi_4O_5Br_2$ microspheres as observed in the FESEM image **(Fig. 3)**. However, 1%wt-$FeVO_4/Bi_4O_5Br_2/BiOBr$ exhibited the highest photocatalytic activity, suggesting that the

surface area and pore volume were not the main factor enhancing its photocatalytic performance. Therefore, the enhanced photocatalytic activity of the ternary 1%wt-$FeVO_4/Bi_4O_5Br_2$/BiOBr heterojunction could be ascribed to its improved optical and electrochemical properties upon coupling $Bi_4O_5Br_2$/BiOBr with $FeVO_4$.

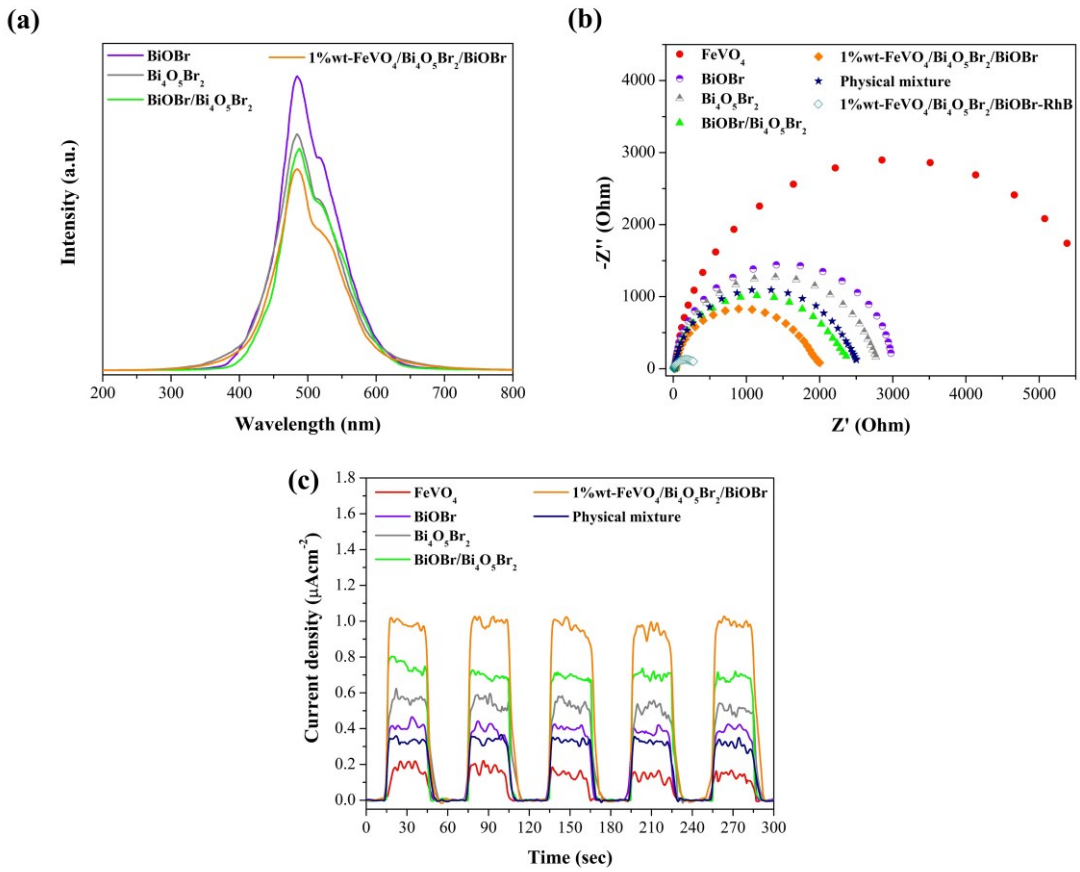

Fig. 10. (a) PL emission spectra, (b) EIS Nyquist plots and (c) photocurrent responses of the photocatalyst samples.

3.8. Charge transfer and photocatalytic mechanisms

Mott-Schottky measurements were performed to determine band potentials and the electrically conductive nature of the single materials. As illustrated in **Fig. 11**, positive slopes were observed for the BiOBr, $Bi_4O_5Br_2$ and $FeVO_4$ electrodes indicating that these materials are an n-type semiconductor [71,72]. The flat band potentials (E_{FB}) were 0.068, -0.050, and -

0.53 V (*vs.* NHE, pH = 0) for BiOBr, $Bi_4O_5Br_2$ and $FeVO_4$, respectively. Generally, E_{FB} of the n-type semiconductor was approximately -0.1 below its conduction band potential (E_{CB}) [71,73]. Thereby, E_{CB} of BiOBr, $Bi_4O_5Br_2$ and $FeVO_4$ could be determined as -0.032, -0.15, and -0.63 V (*vs.* NHE, pH = 0), respectively. According to the Tauc' plots shown in **Fig. 5**(b), the valence band potentials (E_{VB}) of BiOBr, $Bi_4O_5Br_2$, and $FeVO_4$ were 2.898, 2.45, and 1.45 V (*vs.* NHE, pH = 0), respectively.

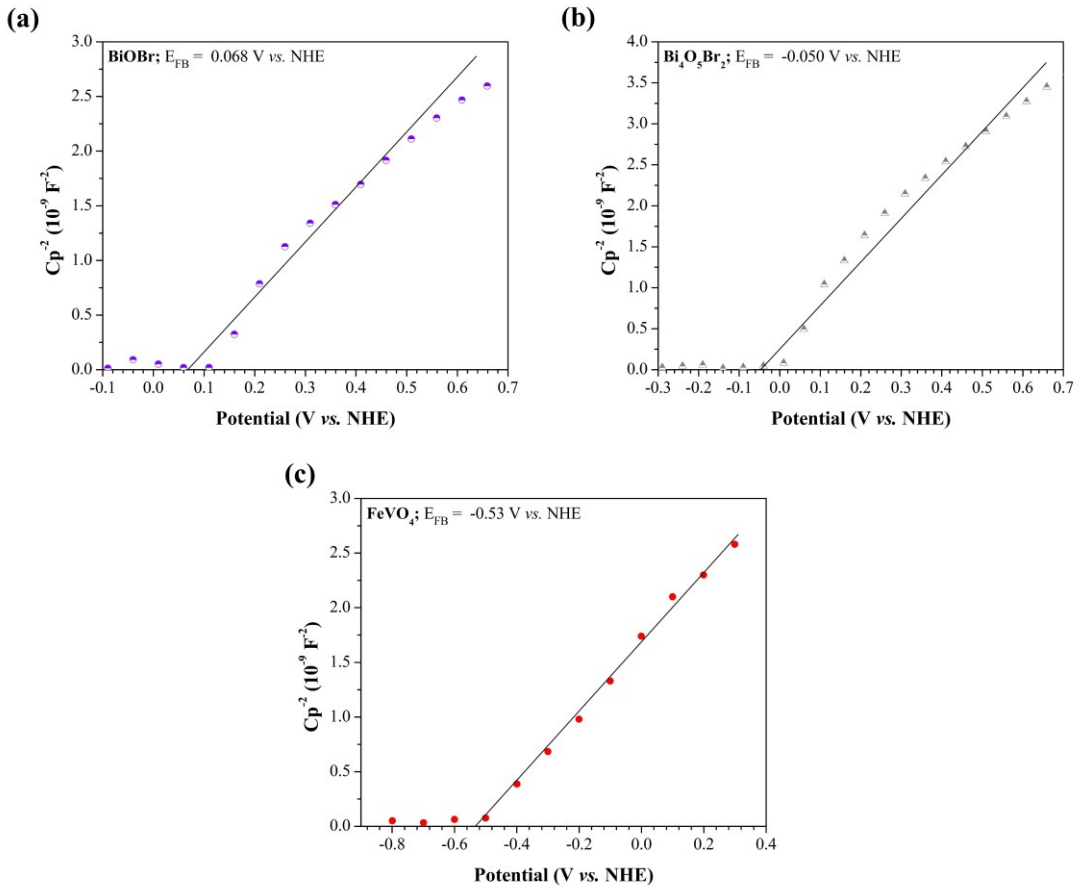

Fig. 11. Mott-Schottky plots of (a) BiOBr, (b) $Bi_4O_5Br_2$ and (c) $FeVO_4$.

In order to fully realize the photocatalytic mechanism, the active species generated during the photocatalytic RhB degradation process were identified by trapping experiments. **Fig. 12**(a) shows the effect of different scavengers on RhB photodegradation over the binary BiOBr/Bi_4OBr_2 heterojunction photocatalyst. The photodegradation efficiency of RhB

significantly decreased with the addition of EDTA-2Na or $K_2Cr_2O_7$ demonstrating that h^+ and e^- are mainly responsible for RhB degradation. The photodegradation efficiency moderately decreased by 30% in the presence of ASC, implying that $O_2^{\bullet-}$ was also one of the active species involved in the photocatalytic reaction; however, it was not determined to be a main active specie. On the contrary, the degradation efficiency changed slightly after adding isopropanol, implying that $HO^\bullet$ was not involved in the photocatalytic reaction.

The main active species responsible for the photocatalytic degradation of RhB over the ternary 1%wt-$FeVO_4/Bi_4O_5Br_2/BiOBr$ heterojunction photocatalyst was also identified by a series of trapping experiments that employed the same approach. As is presented in **Fig. 12**(b), the photodegradation of RhB was completely inhibited in the presence of EDTA-2Na, demonstrating that h^+ was the main active specie. Similarly, the photodegradation efficiencies remarkably decreased after adding ASC and $K_2Cr_2O_7$, suggesting the importance of both $O_2^{\bullet-}$ and e^- for RhB degradation. In the presence of isopropanol, a negligible change in photo-efficiency was observed. This would indicate that $HO^\bullet$ was almost negligibly active specie in the reaction. The generation of $HO^\bullet$ radicals was verified using the TA-PL probing technique by employing terephthalic acid (5.00×10^{-4} mol L^{-1}) as a molecular probe. Accordingly, the terephthalic acid reacted with $HO^\bullet$ and generated 2-hydroxyterephthalic acid (TAOH) which emitted an intense flurescence at 425 nm with an excitation wavelength of 315 nm. The intensity of TAOH was proportional to the amount of $HO^\bullet$ produced. **Fig. S16** reveals that the emission intensities of TAOH were very low, and the peak intensities of TAOH at prolonged reaction times were just a little bit higher. This supports the understanding that a small amount of $HO^\bullet$ radicals were produced during the photocatalytic process, which agrees well with the trapping experimental result. For the Cr(VI) photoreduction over 1%wt-$FeVO_4/Bi_4O_5Br_2/BiOBr$ (**Fig. 12**(c)), the introduction of $K_2S_2O_8$ resulted in a complete

termination of the reaction indicating that photoactivated electrons were essential for Cr(VI) photoreduction [74].

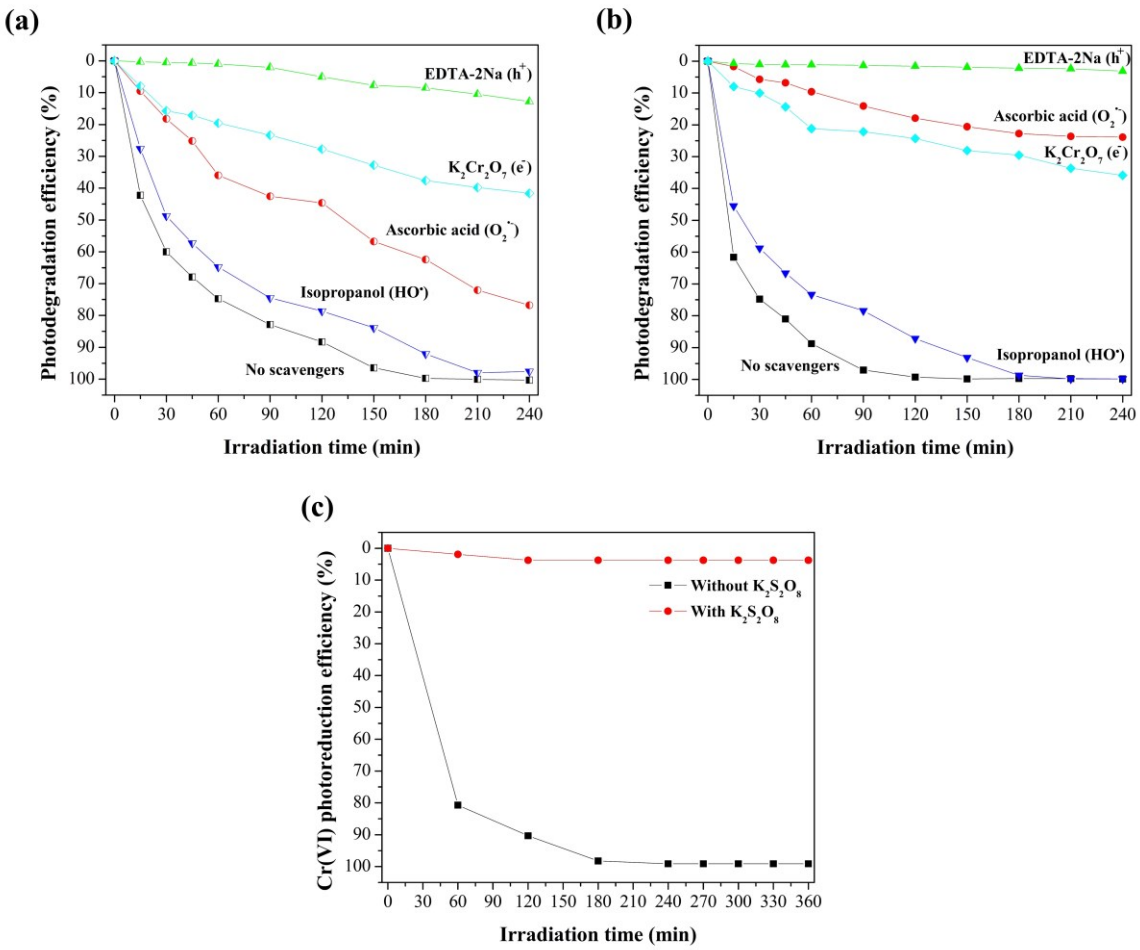

Fig. 12. Effect of scavengers on the photodegradation of RhB by (a) BiOBr/$Bi_4O_5Br_2$ and (b) 1%wt-$FeVO_4$/$Bi_4O_5Br_2$/BiOBr, and (c) the photoreduction of Cr(VI) (20 ppm) by 1%wt-$FeVO_4$/$Bi_4O_5Br_2$/BiOBr under the solution pH of 3.

As shown in **Fig. 12**, the role of $O_2^{\bullet-}$ was more predominant in the ternary $FeVO_4$/$Bi_4O_5Br_2$/BiOBr heterojunction system relative to the binary BiOBr/$Bi_4O_5Br_2$ heterojunction system. This would suggest that a larger number of $O_2^{\bullet-}$ radicals were involved in the RhB degradation process over the ternary heterojunction. The amount of $O_2^{\bullet-}$ generated from the photocatalyst during the photocatalytic reaction was thereby quantitatively determined using the nitrotetrazolium blue (NBT) transformation method [40]. By employing

nitrotetrazolium blue chloride (1.25 x 10^{-5} mol L^{-1}) as a molecular probe, the generated $O_2^{\bullet-}$ radicals reacted with NBT with a reaction molar ratio of 1:4 to form the formazan derivative in the aqueous solution [29]. When the monitoring of this reaction was accomplished with the use of the UV-vis spectrophotometer, the transformation percentage of NBT could be calculated from a decrease in the absorption intensity of the NBT supernatant solutions at λ_{max} of 265 nm. This decrease in intensity would indicate the presence of a higher degree of NBT transformation, which correlated to an increase in the generated $O_2^{\bullet-}$ radicals. **Fig. 13**(a) and **Fig. S17** clearly show that the single BiOBr photocatalyst exhibited lower NBT transformation percentage (8.1%) than that of $Bi_4O_5Br_2$ (13.4%). This would suggest that electrons in CB of BiOBr have lower reduction potential to reduce dissolved O_2 to $O_2^{\bullet-}$. For the binary BiOBr/$Bi_4O_5Br_2$ photocatalyst, the transformation percentage of NBT was higher (21.1%) than in the single photocatalysts. This suggests a higher amount of $O_2^{\bullet-}$ was produced during the photocatalysis. Among the other photocatalysts, 1%wt-$FeVO_4$/$Bi_4O_5Br_2$/BiOBr provided the greatest NBT transformation percentage (30.4%). The amounts of generated $O_2^{\bullet-}$ radicals, calculated from the NBT transformation experiments, were 2.1, 4.7, 7.8, 10.8, and 16.3 μmol L^{-1} for $FeVO_4$, BiOBr, $Bi_4O_5Br_2$, BiOBr/$Bi_4O_5Br_2$, and 1%wt-$FeVO_4$/$Bi_4O_5Br_2$/BiOBr, respectively (**Fig. 13**(b)). The higher $O_2^{\bullet-}$ production efficiency of the binary and ternary heterojunction photocatalysts indicated improved segregation and migration processes of the charge carriers between the interface of the constituent semiconductors in the heterojunctions. Interestingly, the addition of RhB in the reaction system greatly improved both the NBT transformation percentage (30.4%) and the $O_2^{\bullet-}$ yield (34.3 μmolL^{-1}). This result further supports the essential role of RhB as a photosensitizer during the photocatalytic reaction. In addition, RhB could capture photogenerated holes [75–77], decreasing the overall recombination of electron-hole pair in the ternary heterostructure and improving the charge transfer efficiency [78]. Consequently, a large number of electrons could be photogenerated

and react to the dissolved O_2 in the solution to yield $O_2^{\bullet-}$ during the photocatalysis. The impressive increase in the production of reactive $O_2^{\bullet-}$ resulted in an outperforming photocatalytic process.

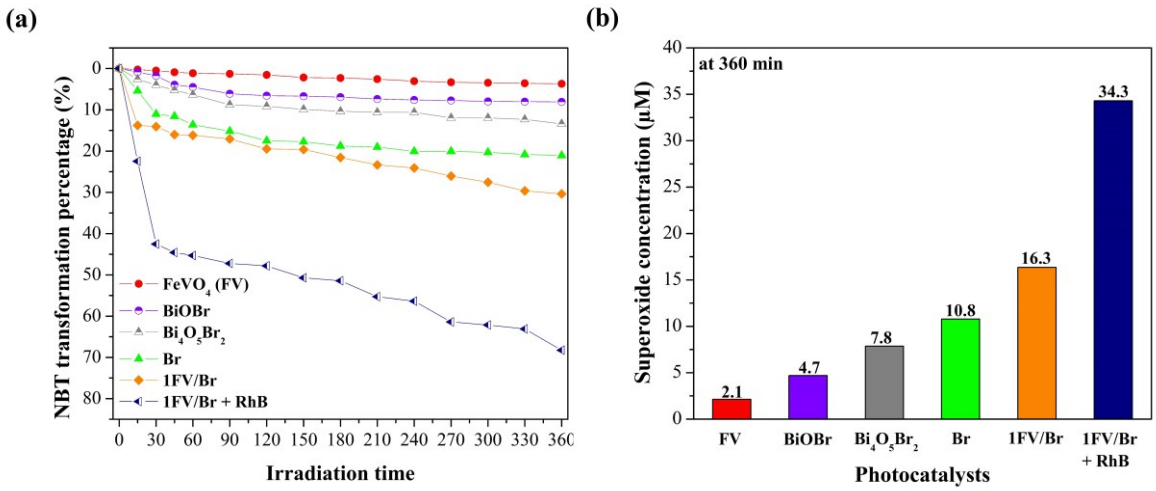

Fig. 13. (a) NBT transformation percentage and (b) concentration of $O_2^{\bullet-}$ radicals generated after 360 min of visible light irradiation over the single, binary, and ternary photocatalysts.

According to the results from the Mott-Schottky plots, active species trapping experiments, and the NBT transformation experiment, two possible charge transfer pathways over the binary BiOBr/$Bi_4O_5Br_2$ heterojunction photocatalyst have been proposed in the first step. As has been illustrated in **Scheme S1**, the band potentials of BiOBr and $Bi_4O_5Br_2$ were aligned in a staggered manner, driving the migration of the charge carrier that was proceeded via the conventional type-II (**Scheme S1**(a)) or direct Z-scheme (**Scheme S1**(b)) mechanisms. Under visible light irradiation, both BiOBr and $Bi_4O_5Br_2$ were excited to yield electrons and holes on their CB and VB. In the conventional type-II mechanism, the excited electrons transferred from CB of $Bi_4O_5Br_2$ (-0.15 V *vs.* NHE) to CB of BiOBr (-0.032 V *vs.* NHE) while holes transfer from VB of BiOBr (2.898 V *vs.* NHE) to VB of $Bi_4O_5Br_2$ (2.45 V *vs.* NHE). This charge transfer pathway resulted in low reducibility and oxidizability of the binary BiOBr/$Bi_4O_5Br_2$ heterojunction. Furthermore, the potential of the accumulated electrons on CB

of BiOBr were at a lower band position than the reduction potential of $O_2/O_2^{\bullet-}$ (-0.046 V *vs.* NHE). Hence, these electrons could not reduce O_2 to $O_2^{\bullet-}$ radicals, which is contrary to the results from the active species trapping and NBT transformation experiments. For the direct Z-scheme mechanism, the photoactivated electrons at CB of BiOBr were transferred to combine with holes in VB of $Bi_4O_5Br_2$, thus preserving a strong reducibility of electrons accumulated in CB of $Bi_4O_5Br_2$, and thereby decreasing the probability of electron-hole pair recombination within the constituent photocatalysts. As a result, the strong reducing electrons in CB of $Bi_4O_5Br_2$ could react with O_2 to produce $O_2^{\bullet-}$. In the meantime, the strong oxidizing holes that remained in VB of BiOBr could directly degrade RhB molecules [79,80].

After introducing $FeVO_4$ into the binary BiOBr/$Bi_4O_5Br_2$ heterostructure, the ternary $FeVO_4$/$Bi_4O_5Br_2$/BiOBr heterostructure was constructed. The charge transfer pathway in the ternary heterojunction system could then be proposed by the same approach as the binary BiOBr/$Bi_4O_5Br_2$ heterostructure system. As is shown in **Scheme S2**, $FeVO_4$ was also activated by visible light, generating electrons and holes at its CB and VB, respectively. The electrons accumulated at CB of $Bi_4O_5Br_2$ in the binary BiOBr/$Bi_4O_5Br_2$ heterostructure could migrate to VB of $FeVO_4$ through the Z-scheme charge transfer process. With regard to this mechanism, the photoactivated electrons in CB of $FeVO_4$ (-0.63 V *vs.* NHE) possessed the highest reduction potential when compared with BiOBr (-0.032V *vs*. NHE) and $Bi_4O_5Br_2$ (-0.15 V *vs*. NHE). As a result, remarkably higher amounts of $O_2^{\bullet-}$ were generated as was proven by the active species trapping (**Fig. 12**) and NBT transformation (**Fig. 13**) experiments. Thus, the charge transfer in the ternary $FeVO_4$/BiOBr/$Bi_4O_5Br_2$ heterostructure was proposed to be a double Z-scheme mechanism.

The silver (Ag) photo-deposition experiment was carried out to confirm the double Z-scheme charge transfer pathway, where the photoactivated electrons were left in CB of $FeVO_4$. HRTEM image of the $FeVO_4$ nanoparticles in the ternary 1%wt-$FeVO_4$/$Bi_4O_5Br_2$/BiOBr

heterostructure (**Fig. S18**) indicates that there were Ag nanoparticles with a lattice fringe of 0.231 nm, which corresponded to (111) plane of Ag that was deposited on the surface of $FeVO_4$. This result indicated that the reduction of Ag^+ under visible light irradiation occurred on the surface of $FeVO_4$ rather than on the surface of $BiOBr/Bi_4O_5Br_2$ nanoparticles. Furthermore, the sensitization mechanism trigged by RhB was found to be involved in the charge transfer process. After irradiation by visible light, RhB molecules were also brought to an excited states (RhB*). The excited electrons in the LUMO of RhB* (-1.42 V *vs.* NHE) could be injected into CB of $FeVO_4$ with a higher favorability than either BiOBr or $Bi_4O_5Br_2$. This was due to the more negative E_{CB} value of $FeVO_4$ [81]. The RhB photosensitization resulted in an accumulation of electrons in CB of $FeVO_4$ which favored $O_2^{\bullet-}$ generation (**Scheme S2**). According to the above discussion, a photocatalytic mechanism for the simultaneous Cr(VI) reduction and RhB degradation in the Cr(VI)/RhB combined pollutant system over the ternary heterojunction photocatalyst is presented in **Scheme 1**. RhB molecules not only act as an efficient photosensitizer to increase electron concentrations injected into the ternary heterojunction during photocatalytic reaction but they also act as a hole capturing agent [75–77] by consuming the photocatalytically generated holes in VB of BiOBr. As a result, the production of photoactivated electrons, which are essential for Cr(VI) photoreduction, is further improved to promote the photoreduction of Cr(VI).

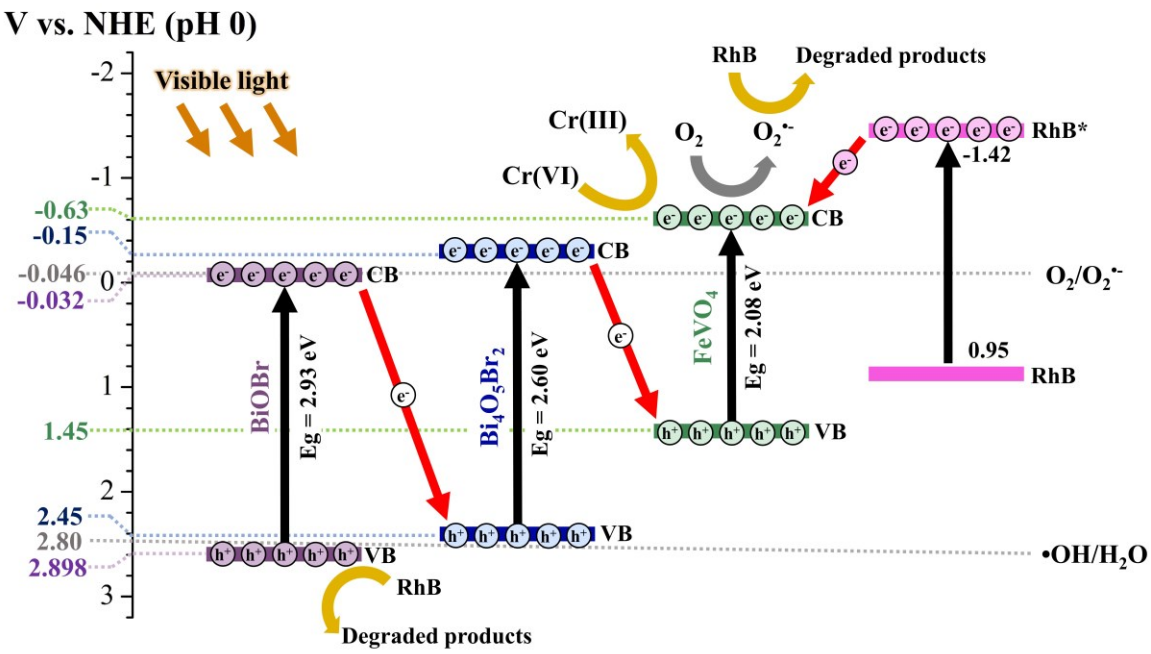

Scheme 1. Proposed charge transfer and photocatalytic mechanisms for simultaneous removal of Cr(VI) and RhB in the Cr(VI) and RhB co-exist system over the ternary $FeVO_4/Bi_4O_5Br_2/BiOBr$ heterojunction photocatalyst.

4. Conclusion

Novel $FeVO_4/Bi_4O_5Br_2/BiOBr$ ternary heterostructures with different $FeVO_4$ contents were successfully synthesized by the facial one-step microwave irradiation method, followed by the wet-impregnation process. Among other synthesized photocatalysts, 1%wt-$FeVO_4/Bi_4O_5Br_2/BiOBr$ displayed the maximum photocatalytic activity toward degrading rhodamine B (RhB), methylene blue (MB) and salicylic acid (SA), and reducing hexavalent chromium (Cr(VI)) with the removal rates of approximately 20, 5, 8, and 89 times higher than those of commercial TiO_2 P25, respectively. In the Cr(VI)/RhB combined pollutant system, the presence of RhB molecules synergically increased the Cr(VI) photoreduction efficiency through the RhB-sensitization and photogenerated hole consuming processes. This would in turn increase electron concentrations in the ternary heterojunction system and $O_2^{\bullet-}$ radicals, as evidenced by the trapping experiments, electron-impedance spectroscopy and nitrotetrazolium

blue transformation studies. The adsorption abilities of the dyes on the surface of the ternary photocatalyst with negatively charged zeta potential was required to initiate dye-sensitization. In comparison with the single and binary photocatalysts, the boosted photocatalytic activity and long-term photostability in the acidic conditions of the ternary heterojunction photocatalyst were attributed to the improved visible light absorption, and the highly efficient segregation and migration of the charge carriers through the double Z-scheme mechanism. These outcomes resulted from the intimate interfacial contact between the three different semiconductor phases. Practical applications of the ternary heterojunction photocatalysts in real wastewater containing both Cr(VI) and RhB, as well as common inorganic anions existing in polluted water, require further studies. However, this research has produced the promising directions to remediate organic substances and heavy metal-contaminated water.

Credit author statement

Auttaphon Chachvalvutikul: Conceptualization; Methodology; Formal analysis; Investigation; Writing - Original draft; Writing - review & editing; Visualization. **Tawanwit Luangwanta:** Formal analysis; Investigation. **Sulawan Kaowphong:** Conceptualization; Methodology; Validation; Investigation; Resources; Writing - original draft; Writing - review & editing; Visualization; Supervision; Project administration; Funding acquisition.

Declaration of interests

The authors declare that there are no conflicts of interest.

Acknowledgements

This research project is supported by TSRI, and partially supported by Chiang Mai University.

References

[1] X. Liu, H. Pang, X. Liu, Q. Li, N. Zhang, L. Mao, M. Qiu, B. Hu, H. Yang, X. Wang, Orderly Porous Covalent Organic Frameworks-based Materials : Superior Adsorbents for Pollutants Removal from Aqueous Solutions, Innov. 2 (2021) 100076. https://doi.org/10.1016/j.xinn.2021.100076.

[2] X. Liu, R. Ma, L. Zhuang, B. Hu, J. Chen, X. Liu, Recent developments of doped g-C_3N_4 photocatalysts for the degradation of organic pollutants, Crit. Rev. Environ. Sci. Technol. 51 (2021) 751–790. https://doi.org/10.1080/10643389.2020.1734433.

[3] M. Hao, M. Qiu, H. Yang, B. Hu, X. Wang, Recent advances on preparation and environmental applications of MOF-derived carbons in catalysis, Sci. Total Environ. 760 (2021) 143333. https://doi.org/10.1016/j.scitotenv.2020.143333.

[4] S. Dong, J. Feng, M. Fan, Y. Pi, L. Hu, X. Han, M. Liu, J. Sun, J. Sun, Recent developments in heterogeneous photocatalytic water treatment using visible light-responsive photocatalysts: A review, RSC Adv. 5 (2015) 14610–14630. https://doi.org/10.1039/c4ra13734e.

[5] A. Hernández-Ramírez, I. Medina-Ramírez, Photocatalytic Semiconductors, Springer, Switzerland, 2015. https://doi.org/10.1007/978-3-319-10999-2.

[6] J. Di, J. Xia, H. Li, S. Guo, S. Dai, Bismuth oxyhalide layered materials for energy and environmental applications, Nano Energy. 41 (2017) 172–192. https://doi.org/10.1016/j.nanoen.2017.09.008.

[7] Z. Liu, J. Niu, P. Feng, Y. Zhu, Solvothermal synthesis of $Bi_{24}O_{31}Cl_xBr_{10-x}$ solid solutions with enhanced visible light photocatalytic property, Ceram. Int. 41 (2015) 4608–4615. https://doi.org/10.1016/j.ceramint.2014.12.004.

[8] A.M. Ganose, M. Cuff, K.T. Butler, A. Walsh, D.O. Scanlon, Interplay of Orbital and

Relativistic Effects in Bismuth Oxyhalides: BiOF, BiOCl, BiOBr, and BiOI, Chem. Mater. 28 (2016) 1980–1984. https://doi.org/10.1021/acs.chemmater.6b00349.

[9] L. Yao, H. Yang, Z. Chen, M. Qiu, B. Hu, X. Wang, Bismuth oxychloride-based materials for the removal of organic pollutants in wastewater, Chemosphere. 273 (2021) 128576. https://doi.org/10.1016/j.chemosphere.2020.128576.

[10] L. Chen, R. Huang, M. Xiong, Q. Yuan, J. He, J. Jia, M.Y. Yao, S.L. Luo, C.T. Au, S.F. Yin, Room-temperature synthesis of flower-like BiOX (X=Cl, Br, I) hierarchical structures and their visible-light photocatalytic activity, Inorg. Chem. 52 (2013) 11118–11125. https://doi.org/10.1021/ic401349j.

[11] J. Lv, Q. Hu, C. Cao, Y. Zhao, Modulation of valence band maximum edge and photocatalytic activity of BiOX by incorporation of halides, Chemosphere. 191 (2018) 427–437. https://doi.org/10.1016/j.chemosphere.2017.09.149.

[12] H. An, D.U. Yi, T.M. Wang, C. Wang, W. Hao, J. Zhang, Photocatalytic properties of BiOX (X = Cl, Br, and I), Rare Met. 27 (2008) 243–250. https://doi.org/10.1016/S1001-0521(08)60123-0.

[13] I.D. Sharma, G.K. Tripathi, V.K. Sharma, S.N. Tripathi, R. Kurchania, C. Kant, A.K. Sharma, K.K. Saini, One-pot synthesis of three bismuth oxyhalides (BiOCl, BiOBr, BiOI) and their photocatalytic properties in three different exposure conditions, Cogent Chem. 1 (2015) 1–15. https://doi.org/10.1080/23312009.2015.1076371.

[14] D. Kato, K. Hongo, R. Maezono, M. Higashi, H. Kunioku, M. Yabuuchi, H. Suzuki, H. Okajima, C. Zhong, K. Nakano, R. Abe, H. Kageyama, Valence Band Engineering of Layered Bismuth Oxyhalides toward Stable Visible-Light Water Splitting: Madelung Site Potential Analysis, J. Am. Chem. Soc. 139 (2017) 18725–18731. https://doi.org/10.1021/jacs.7b11497.

[15] X. Jin, L. Ye, H. Xie, G. Chen, Bismuth-rich bismuth oxyhalides for environmental and

energy photocatalysis, Coord. Chem. Rev. 349 (2017). https://doi.org/10.1016/j.ccr.2017.08.010.

[16] G. Wu, Y. Zhao, Y. Li, B. Souvanhthong, H. Ma, J. Zhao, Facile aqueous synthesis of $Bi_4O_5Br_2$ nanosheets for improved visible-light photocatalytic activity, Ceram. Int. 44 (2018) 5392–5401. https://doi.org/10.1016/j.ceramint.2017.12.168.

[17] X. Zhang, P. Yang, B. Yang, Y. Bai, W. Liu, K. Zhang, Synthesis of the composite catalyst $Bi_4O_5Br_2$/BiOBr for the improved photocatalytic degradation of oilfield produced wastewater, J. Mater. Sci. Mater. Electron. 30 (2019) 17276–17287. https://doi.org/10.1007/s10854-019-02074-6.

[18] R. Li, F. Xie, J. Liu, Y. Wang, Y. Wang, X. Zhang, C. Fan, Synthesis of $Bi_4O_5Br_2$ from reorganization of BiOBr and its excellent visible light photocatalytic activity, Dalt. Trans. 45 (2016) 9182–9186. https://doi.org/10.1039/c6dt00997b.

[19] J. Xu, Y.G. Mao, T. Liu, Y. Peng, Synthesis of a novel one-dimensional BiOBr-$Bi_4O_5Br_2$ heterostructure with a high quality interface and its enhanced visible-light photocatalytic activity, CrystEngComm. 20 (2018) 2292–2298. https://doi.org/10.1039/c8ce00157j.

[20] X. Su, D. Wu, Facile construction of the phase junction of BiOBr and $Bi_4O_5Br_2$ nanoplates for ciprofloxacin photodegradation, Mater. Sci. Semicond. Process. 80 (2018) 123–130. https://doi.org/10.1016/j.mssp.2018.02.034.

[21] X. Jin, C. Lv, X. Zhou, H. Xie, S. Sun, Y. Liu, Q. Meng, G. Chen, A bismuth rich hollow $Bi_4O_5Br_2$ photocatalyst enables dramatic CO2 reduction activity, Nano Energy. 64 (2019) 103955. https://doi.org/10.1016/j.nanoen.2019.103955.

[22] J. Zhao, M. Ji, J. Di, Y. Ge, P. Zhang, J. Xia, H. Li, Synthesis of g-C_3N_4/$Bi_4O_5Br_2$ via reactable ionic liquid and its cooperation effect for the enhanced photocatalytic behavior towards ciprofloxacin degradation, J. Photochem. Photobiol. A Chem. 347 (2017) 168–

176. https://doi.org/10.1016/j.jphotochem.2017.07.023.

[23] P. Li, W. Cao, Y. Zhu, Q. Teng, L. Peng, C. Jiang, C. Feng, Y. Wang, NaOH-induced formation of 3D flower-sphere BiOBr/$Bi_4O_5Br_2$ with proper-oxygen vacancies via in-situ self-template phase transformation method for antibiotic photodegradation, Sci. Total Environ. 715 (2020) 136809. https://doi.org/10.1016/j.scitotenv.2020.136809.

[24] J. Xu, Y.G. Mao, T. Liu, Y. Peng, Synthesis of a novel one-dimensional BiOBr-$Bi_4O_5Br_2$ heterostructure with a high quality interface and its enhanced visible-light photocatalytic activity, CrystEngComm. 20 (2018) 2292–2298. https://doi.org/10.1039/c8ce00157j.

[25] M. Li, Y. Cui, Y. Jin, H. Li, Facile hydrolysis synthesis of $Bi_4O_5Br_2$ photocatalyst with excellent visible light photocatalytic performance for the degradation of resorcinol, RSC Adv. 6 (2016) 47545–47551. https://doi.org/10.1039/c6ra07386g.

[26] C. Zheng, G. He, X. Xiao, M. Lu, H. Zhong, X. Zuo, J. Nan, Selective photocatalytic oxidation of benzyl alcohol into benzaldehyde with high selectivity and conversion ratio over $Bi_4O_5Br_2$ nanoflakes under blue LED irradiation, Appl. Catal. B Environ. 205 (2017) 201–210. https://doi.org/10.1016/j.apcatb.2016.12.026.

[27] Y. Bai, T. Chen, P. Wang, L. Wang, L. Ye, Bismuth-rich $Bi_4O_5X_2$ (X = Br, and I) nanosheets with dominant {1 0 1} facets exposure for photocatalytic H2 evolution, Chem. Eng. J. 304 (2016) 454–460. https://doi.org/10.1016/j.cej.2016.06.100.

[28] Y. Bai, P. Yang, L. Wang, B. Yang, H. Xie, Y. Zhou, L. Ye, Ultrathin $Bi_4O_5Br_2$ nanosheets for selective photocatalytic CO_2 conversion into CO, Chem. Eng. J. 360 (2019) 473–482. https://doi.org/10.1016/j.cej.2018.12.008.

[29] D. Majhi, K. Das, A. Mishra, R. Dhiman, B.G. Mishra, One pot synthesis of CdS/BiOBr/$Bi_2O_2CO_3$: A novel ternary double Z-scheme heterostructure photocatalyst for efficient degradation of atrazine, Appl. Catal. B Environ. 260 (2020) 118222.

https://doi.org/10.1016/j.apcatb.2019.118222.

[30] S. Heidari, M. Haghighi, M. Shabani, Sunlight-activated BiOCl/BiOBr–$Bi_{24}O_{31}Br_{10}$ photocatalyst for the removal of pharmaceutical compounds, J. Clean. Prod. 259 (2020) 120679. https://doi.org/10.1016/j.jclepro.2020.120679.

[31] Y. Yu, P. Ju, D. Zhang, X. Han, X. Yin, L. Zheng, C. Sun, Peroxidase-like activity of $FeVO_4$ nanobelts and its analytical application for optical detection of hydrogen peroxide, Sensors Actuators B Chem. 233 (2016) 162–172. https://doi.org/10.1016/j.snb.2016.04.041.

[32] B. Ozturk, G.S. Pozan Soylu, Synthesis of surfactant-assisted $FeVO_4$ nanostructure: Characterization and photocatalytic degradation of phenol, J. Mol. Catal. A Chem. 398 (2015) 65–71. https://doi.org/10.1016/j.molcata.2014.11.013.

[33] A. Chachvalvutikul, J. Jakmunee, S. Thongtem, S. Kittiwachana, S. Kaowphong, Novel $FeVO_4/Bi_7O_9I_3$ nanocomposite with enhanced photocatalytic dye degradation and photoelectrochemical properties, Appl. Surf. Sci. 475 (2019) 175–184. https://doi.org/10.1016/j.apsusc.2018.12.214.

[34] A. Chachvalvutikul, S. Kaowphong, Direct Z-scheme $FeVO_4$/BiOCl heterojunction as a highly efficient visible-light-driven photocatalyst for photocatalytic dye degradation and Cr(VI) reduction, Nanotechnology. 31 (2020). https://doi.org/10.1088/1361-6528/ab61d1.

[35] Q. Wang, X. Chen, K. Yu, Y. Zhang, Y. Cong, Synergistic photosensitized removal of Cr(VI) and Rhodamine B dye on amorphous TiO_2 under visible light irradiation, J. Hazard. Mater. 246–247 (2013) 135–144. https://doi.org/10.1016/j.jhazmat.2012.12.017.

[36] F. Hashemzadeh, A. Gaffarinejad, R. Rahimi, Porous p-NiO/n-Nb_2O_5 nanocomposites prepared by an EISA route with enhanced photocatalytic activity in simultaneous Cr(VI)

reduction and methyl orange decolorization under visible light irradiation, J. Hazard. Mater. 286 (2015) 64–74. https://doi.org/10.1016/j.jhazmat.2014.12.038.

[37] L. Huang, Q. Chan, X. Wu, H. Wang, Y. Liu, The simultaneous photocatalytic degradation of phenol and reduction of Cr (VI) by TiO_2/CNTs, J. Ind. Eng. Chem. 18 (2012) 574–580. https://doi.org/10.1016/j.jiec.2011.11.060.

[38] J. Xu, L. Li, C. Guo, Y. Zhang, S. Wang, Removal of benzotriazole from solution by BiOBr photocatalysis under simulated solar irradiation, Chem. Eng. J. 221 (2013) 230–237. https://doi.org/10.1016/j.cej.2013.01.081.

[39] X. Li, C. Niu, D. Huang, X. Wang, X. Zhang, G. Zeng, Q. Niu, Preparation of magnetically separable Fe_3O_4/BiOI nanocomposites and its visible photocatalytic activity, Appl. Surf. Sci. 286 (2013) 40–46. https://doi.org/10.1016/j.apsusc.2013.08.139.

[40] A. Chachvalvutikul, T. Luangwanta, S. Pattisson, G.J. Hutchings, S. Kaowphong, Enhanced photocatalytic degradation of organic pollutants and hydrogen production by a visible light–responsive Bi_2WO_6/$ZnIn_2S_4$ heterojunction, Appl. Surf. Sci. 544 (2020) 148885. https://doi.org/10.1016/j.apsusc.2020.148885.

[41] C. Zeng, Y. Hu, H. Huang, $BiOBr_{0.75}I_{0.25}$/$BiOIO_3$ as a Novel Heterojunctional Photocatalyst with Superior Visible-Light-Driven Photocatalytic Activity in Removing Diverse Industrial Pollutants, ACS Sustain. Chem. Eng. 5 (2017) 3897–3905. https://doi.org/10.1021/acssuschemeng.6b03066.

[42] N. Chumha, T. Thongtem, S. Thongtem, S. Kittiwachana, S. Kaowphong, Effect of different polyol solvents on the synthesis of $CuInS_2$ nanoparticles by cyclic microwave irradiation, J. Ceram. Process. Res. 18 (2017) 871–874.

[43] S. Samanta, R. Srivastava, Thermal catalysis vs. photocatalysis: A case study with $FeVO_4$/g-C_3N_4 nanocomposites for the efficient activation of aromatic and benzylic C–

H bonds to oxygenated products, Appl. Catal. B Environ. 218 (2017) 621–636. https://doi.org/10.1016/j.apcatb.2017.06.043.

[44] Q. Nong, M. Cui, H. Lin, L. Zhao, Y. He, Fabrication, characterization and photocatalytic activity of g-C_3N_4 coupled with $FeVO_4$ nanorod, RSC Adv. 5 (2015) 27933–27939. https://doi.org/10.1039/C5RA01484K.

[45] X. She, Z. Zhang, M. Baek, K. Yong, Elevated photoelectrochemical activity of $FeVO_4$/$ZnFe_2O_4$ /ZnO branch-structures via slag assisted-synthesis, RSC Adv. 7 (2017) 16787–16794. https://doi.org/10.1039/C7RA00812K.

[46] X. Liu, G. Xie, C. Huang, Q. Xu, Y. Zhang, Y. Luo, A facile method for preparing VO2 nanobelts, Mater. Lett. 62 (2008) 1878–1880. https://doi.org/10.1016/j.matlet.2007.10.022.

[47] J. Gao, Y. Gao, Z. Sui, Z. Dong, S. Wang, D. Zou, Hydrothermal synthesis of BiOBr/$FeWO_4$ composite photocatalysts and their photocatalytic degradation of doxycycline, J. Alloys Compd. 732 (2018) 43–51. https://doi.org/10.1016/j.jallcom.2017.10.092.

[48] Y. Yang, J. Wu, T. Xiao, Z. Tang, J. Shen, H. Li, Y. Zhou, Z. Zou, Urchin-like hierarchical CoZnAl-LDH/RGO/g-C_3N_4 hybrid as a Z-scheme photocatalyst for efficient and selective CO_2 reduction, Appl. Catal. B Environ. 255 (2019) 117771. https://doi.org/10.1016/j.apcatb.2019.117771.

[49] S.R. Zhu, M.K. Wu, W.N. Zhao, F.Y. Yi, K. Tao, L. Han, Fabrication of heterostructured BiOBr/$Bi_{24}O_{31}Br_{10}$/TiO_2 photocatalyst by pyrolysis of MOF composite for dye degradation, J. Solid State Chem. 255 (2017) 17–26. https://doi.org/10.1016/j.jssc.2017.07.038.

[50] K.W. Bladh, M.C. Nichols, M. Data, P. Each, K.W. Bladh, R.A. Bideaux, E. Anthony-morton, G. Barbara, J.W. Anthony, R.A. Bideaux, K.W. Bladh, M.C. Nichols,

Handbook of Mineralogy Crystal Data, Mineral Data Publishing, Virginia, USA, 2010.

[51] Shahid-ul-Islam, Advanced Materials for Wastewater Treatment, 1st ed., Scrivener Publishing, Beverly, Massachusetts, 2017. https://doi.org/10.1002/9781119407805.

[52] G. Wu, Y. Zhao, Y. Li, H. Ma, J. Zhao, pH-dependent synthesis of iodine-deficient bismuth oxyiodide microstructures: Visible-light photocatalytic activity, J. Colloid Interface Sci. 510 (2018) 228–236. https://doi.org/10.1016/j.jcis.2017.09.053.

[53] C.Y. Wang, X. Zhang, H. Bin Qiu, W.K. Wang, G.X. Huang, J. Jiang, H.Q. Yu, Photocatalytic degradation of bisphenol A by oxygen-rich and highly visible-light responsive $Bi_{12}O_{17}Cl_2$ nanobelts, Appl. Catal. B Environ. 200 (2017) 659–665. https://doi.org/10.1016/j.apcatb.2016.07.054.

[54] G. Ji, H. Shen, J. Zhang, A.A. Al-Saadi, X. Chang, M.A. Ali, Q. Zhou, M. Du, Y. Liu, M.A. Gondal, Photodegradation of Rhodamine B over unexcited semiconductor compounds of BiOCl and BiOBr, J. Colloid Interface Sci. 377 (2012) 291–298. https://doi.org/10.1016/j.jcis.2012.03.021.

[55] Y.Y. Lee, J.H. Moon, Y.S. Choi, G.O. Park, M. Jin, L.Y. Jin, D. Li, J.Y. Lee, S.U. Son, J.M. Kim, Visible-Light Driven Photocatalytic Degradation of Organic Dyes over Ordered Mesoporous $Cd_xZn_{1-x}S$ Materials, J. Phys. Chem. C. 121 (2017) 5137–5144. https://doi.org/10.1021/acs.jpcc.7b00038.

[56] J. Jiang, K. Zhao, X. Xiao, L. Zhang, Synthesis and facet-dependent photoreactivity of BiOCl single-crystalline nanosheets, J. Am. Chem. Soc. 134 (2012) 4473–4476. https://doi.org/10.1021/ja210484t.

[57] W. Cui, W. An, L. Liu, J. Hu, Y. Liang, Synthesis of CdS/BiOBr composite and its enhanced photocatalytic degradation for Rhodamine B, Appl. Surf. Sci. 319 (2014) 298–305. https://doi.org/10.1016/j.apsusc.2014.05.179.

[58] Z. Cui, M. Si, Z. Zheng, L. Mi, W. Fa, H. Jia, Preparation and characterization of

Ag_3PO_4/BiOI composites with enhanced visible light driven photocatalytic performance, Catal. Commun. 42 (2013) 121–124. https://doi.org/10.1016/j.catcom.2013.08.011.

[59] C. Zhao, Z. Wang, X. Li, X. Yi, H. Chu, X. Chen, C.C. Wang, Facile fabrication of BUC-21/$Bi_{24}O_{31}Br_{10}$ composites for enhanced photocatalytic Cr(VI) reduction under white light, Chem. Eng. J. (2019) 123431. https://doi.org/10.1016/j.cej.2019.123431.

[60] A.D. Bokare, W. Choi, Chromate-Induced Activation of Hydrogen Peroxide for Oxidative Degradation of Aqueous Organic Pollutants, Environ. Sci. Technol. 44 (2010) 7232–7237. https://doi.org/10.1021/es903930h.

[61] N. Unceta, F. Séby, J. Malherbe, O.F.X. Donard, Chromium speciation in solid matrices and regulation: A review, Anal. Bioanal. Chem. 397 (2010) 1097–1111. https://doi.org/10.1007/s00216-009-3417-1.

[62] Q. Wang, X. Shi, E. Liu, J.C. Crittenden, X. Ma, Y. Zhang, Y. Cong, Facile synthesis of AgI/BiOI-Bi_2O_3 multi-heterojunctions with high visible light activity for Cr(VI) reduction, J. Hazard. Mater. 317 (2016) 8–16. https://doi.org/10.1016/j.jhazmat.2016.05.044.

[63] H. Xu, Z. Wu, M. Ding, X. Gao, Microwave-assisted synthesis of flower-like BN/BiOCl composites for photocatalytic Cr(VI) reduction upon visible-light irradiation, Mater. Des. 114 (2017) 129–138. https://doi.org/10.1016/j.matdes.2016.10.057.

[64] J. Qu, D. Chen, N. Li, Q. Xu, H. Li, J. He, J. Lu, Coral-inspired nanoscale design of porous SnS_2 for photocatalytic reduction and removal of aqueous Cr(VI), Appl. Catal. B Environ. 207 (2017) 404–411. https://doi.org/10.1016/j.apcatb.2017.02.050.

[65] S. Merouani, O. Hamdaoui, F. Saoudi, M. Chiha, Sonochemical degradation of Rhodamine B in aqueous phase : Effects of additives, Chem. Eng. J. 158 (2010) 550–557. https://doi.org/10.1016/j.cej.2010.01.048.

[66] H. Yu, B. Huang, H. Wang, X. Yuan, L. Jiang, Z. Wu, J. Zhang, G. Zeng, Facile construction of novel direct solid-state Z-scheme AgI/BiOBr photocatalysts for highly effective removal of ciprofloxacin under visible light exposure: Mineralization efficiency and mechanisms, J. Colloid Interface Sci. 522 (2018) 82–94. https://doi.org/10.1016/j.jcis.2018.03.056.

[67] S.R. Zhu, Q. Qi, W.N. Zhao, Y. Fang, L. Han, Enhanced photocatalytic activity in hybrid composite combined BiOBr nanosheets and Bi_2S_3 nanoparticles, J. Phys. Chem. Solids. 121 (2018) 163–171. https://doi.org/10.1016/j.jpcs.2018.05.023.

[68] M. Jiang, Y. Shi, J. Huang, L. Wang, H. She, J. Tong, B. Su, Q. Wang, Synthesis of Flowerlike g-C_3N_4/BiOBr with Enhanced Visible Light Photocatalytic Activity for Dye Degradation, Eur. J. Inorg. Chem. 2018 (2018) 1834–1841. https://doi.org/10.1002/ejic.201800110.

[69] S. Wang, X. Yang, X. Zhang, X. Ding, Z. Yang, K. Dai, H. Chen, A plate-on-plate sandwiched Z-scheme heterojunction photocatalyst: BiOBr-Bi_2MoO_6 with enhanced photocatalytic performance, Appl. Surf. Sci. 391 (2017) 194–201. https://doi.org/10.1016/j.apsusc.2016.07.070.

[70] S. Guo, W. Yang, L. You, J. Li, J. Chen, K. Zhou, Simultaneous reduction of Cr(VI) and degradation of tetracycline hydrochloride by a novel iron-modified rectorite composite through heterogeneous photo-Fenton processes, Chem. Eng. J. 393 (2020) 124758. https://doi.org/10.1016/j.cej.2020.124758.

[71] C. Wang, X. Zhang, H. Qiu, G. Huang, H. Yu, $Bi_{24}O_{31}Br_{10}$ nanosheets with controllable thickness for visible – light – driven catalytic degradation of tetracycline hydrochloride, Appl. Catal. B Environ. 205 (2017) 615–623. https://doi.org/10.1016/j.apcatb.2017.01.015.

[72] S. Lia, G. Zhu, Y. Jia, L. Pan, J. Nie, F. Rao, J. Gao, F. Zhang, C. Li, TiO_2 with exposed

(001) facets/$Bi_4O_5Br_2$ nanosheets heterojunction with enhanced photocatalytic for NO removal, Nanotechnology. 31 (2020) 254002. https://doi.org/10.1088/1361-6528/ab7583.

[73] C. Zeng, Y. Hu, Y. Guo, T. Zhang, F. Dong, X. Du, Y. Zhang, H. Huang, Achieving tunable photocatalytic activity enhancement by elaborately engineering composition-adjustable polynary heterojunctions photocatalysts, Appl. Catal. B Environ. 194 (2016) 62–73. https://doi.org/10.1016/j.apcatb.2016.04.036.

[74] J. Yu, S. Zhuang, X. Xu, W. Zhu, B. Feng, J. Hu, Photogenerated electron reservoir in hetero-p-n CuO-ZnO nanocomposite device for visible-light-driven photocatalytic reduction of aqueous Cr(vi), J. Mater. Chem. A. 3 (2015) 1199–1207. https://doi.org/10.1039/c4ta04526b.

[75] Z. Fang, Q. Li, L. Su, J. Chen, K.C. Chou, X. Hou, Efficient synergy of photocatalysis and adsorption of hexavalent chromium and rhodamine B over Al_4SiC_4/rGO hybrid photocatalyst under visible-light irradiation, Appl. Catal. B Environ. 241 (2019) 548–560. https://doi.org/10.1016/j.apcatb.2018.09.074.

[76] Y. Guo, C. Li, Y. Guo, X. Wang, X. Li, Ultrasonic-assisted synthesis of mesoporous g-C_3N_4/Na-bentonite composites and its application for efficient photocatalytic simultaneous removal of Cr(VI) and RhB, Colloids Surfaces A Physicochem. Eng. Asp. 578 (2019) 123624. https://doi.org/10.1016/j.colsurfa.2019.123624.

[77] M. Qiu, Z. Liu, S. Wang, B. Hu, The photocatalytic reduction of U(VI) into U(IV) by ZIF-8/g-C_3N_4 composites at visible light, Environ. Res. (2020) 110349. https://doi.org/10.1016/j.envres.2020.110349.

[78] H. Wang, H. Guo, N. Zhang, Z. Chen, B. Hu, X. Wang, Enhanced Photoreduction of U(VI) on C_3N_4 by Cr(VI) and Bisphenol A: ESR, XPS, and EXAFS Investigation, Environ. Sci. Technol. 53 (2019) 6454–6461. https://doi.org/10.1021/acs.est.8b06913.

[79] A. Chachvalvutikul, W. Pudkon, T. Luangwanta, T. Thongtem, S. Thongtem, S. Kittiwachana, S. Kaowphong, Enhanced photocatalytic degradation of methylene blue by a direct Z-scheme $Bi_2S_3/ZnIn_2S_4$ photocatalyst, Mater. Res. Bull. 111 (2019) 53–60. https://doi.org/10.1016/j.materresbull.2018.10.034.

[80] F. Qiu, W. Li, F. Wang, H. Li, X. Liu, J. Sun, In-situ synthesis of novel Z-scheme SnS_2/BiOBr photocatalysts with superior photocatalytic efficiency under visible light, J. Colloid Interface Sci. 493 (2017) 1–9. https://doi.org/10.1016/j.jcis.2016.12.066.

[81] Y.L. Min, K. Zhang, Y.C. Chen, Y.G. Zhang, Synthesis of novel visible light responding vanadate/TiO_2 heterostructure photocatalysts for application of organic pollutants, Chem. Eng. J. 175 (2011) 76–83. https://doi.org/10.1016/j.cej.2011.09.042.